Full continuum approach for simulating plume-surface interaction in planetary landings

Omid Ejtehadi[a,b], Rho Shin Myong (명노신)[c], Ilyoup Sohn (손일엽)[d], Byoung Jae Kim (김병재)[a*]*

[a] *School of Mechanical Engineering, Chungnam National University, 99 Daehak-ro, Yuseong-gu, Daejeon 34134, Republic of Korea*

[b] *Institute for Materials and Processes, School of Engineering, University of Edinburgh, Sanderson Building, King's Buildings, Robert Stevenson Road, Edinburgh, EH9 3FB, UK*

[c] *School of Mechanical and Aerospace Engineering, and ACTRC, Gyeongsang National University, Jinju, Gyeongnam 52828, Republic of Korea*

[d] *Intelligent Simulation Center, Korea Institute of Science and Technology Information (KISTI), Daejeon 305806, Republic of Korea*

*Corresponding authors:
Tel +82 42 821-5645; bjkim@cnu.ac.kr
Tel +82 42 869-1635; sohniy@kisti.re.kr

Abstract A high-fidelity computational framework for predicting the interaction of a rocket plume with a dust blanket in an almost vacuum ambient that represents the descent/ascend phase of planetary landing is developed. Compared to the existing continuum frameworks, the developed tool benefits from nonlinear-coupled constitutive relationships obtained using a method of moments approach to tackle the non-equilibrium effects in the rarefied condition. The two-phase flow is modeled in a Eulerian framework that allows for the simulation of a wider range of solid regimes compared to the Lagrangian counterpart. Simulations were conducted to analyze the cratering phenomena and regolith ejecta dynamics. Moreover, the vorticity growth rates were analyzed using a new vorticity transport equation (VTE) by including the bulk viscosity and multiphase terms to demonstrate the contribution of each term to the formation of counter-intuitive festooned patterns on the surface owing to jet impingement. This analysis identified a new contributing mechanism responsible for the scour patterns. Although all the investigated terms in the VTE contribute to such patterns, the viscous term has more effect during the entire investigation period. Furthermore, studies on particulate loading, particle diameter, and bed height were conducted to highlight the role of these parameters on brownout phenomena and scour formation patterns. The simulation results depict that the generated vortex core beneath the nozzle is highly dependent on the diameter of

the particles as well as the bed height: an increase in the height of the bed and particle diameter can lead to a more favorable brownout status.

Keywords: Lunar landing, Two-fluid model, Shock-particle interaction, Rarefaction

I. INTRODUCTION

With the recent developments in planetary explorations to the Moon, Mars, and their comets and asteroids planned by major space organizations, research on expanding the understanding of the challenges and finding solutions to removing the obstacles has increased. Planetary explorations, such as Moon landing, has several stages including launching from the earth, Earth-Moon transfer, circumlunar orbit, and the final powered descent phase.[1] The main aim of this study is the analysis of soft landing, in which the rocket plume impingement on a dusty surface causes erosion and dispersal of the solid particles into the flow field. This leads to severe consequences ranging from blocking the pilot's vision to false sensor and instrument readings. Additionally, dust particles may hit the lunar lander or the previously established sites and instruments near the landing location. A schematic of the problem is shown in **Fig. 1**.

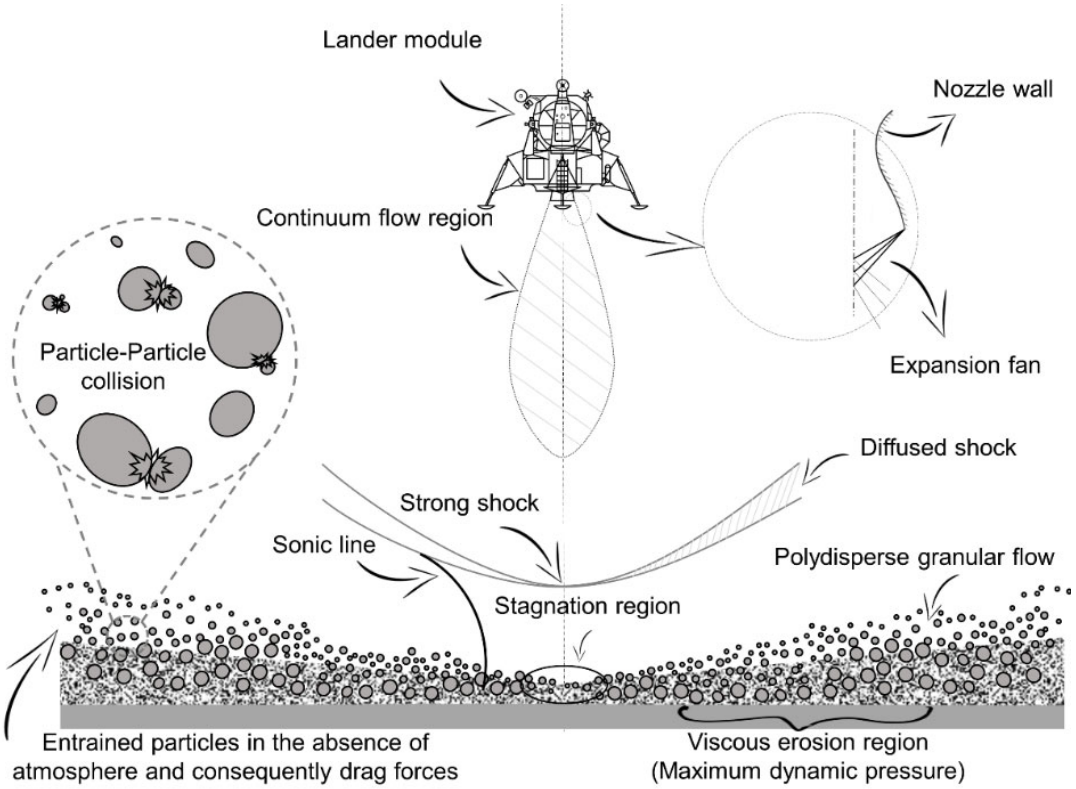

Fig. 1. Schematic of the impingement of engine plume and the subsequent dusty gas flow formed by the ejection of solid particles from the regolith during lunar landing. Reproduced with permission from A. Rahimi, O. Ejtehadi, K.H. Lee, R.S. Myong, Near-field plume-surface interaction and regolith erosion and dispersal during the lunar landing, Acta Astronautica, 175 (2020) 308-326. ©2018 Elsevier.

The study of plume surface interaction (PSI) is a challenging problem with various aspects to be considered. NASA has established a PSI project to expand the current understanding of the problem experimentally and numerically. Furthermore, various theoretical studies have been conducted in the last two decades, which expand on developing methods and tools for understanding the rarefied gas and solid particles interaction. Examples include the pioneering works of Burt and Boyd[2] and Gimelshein *et al.*[3] to extend the direct simulation Monte Carlo (DSMC) method to solve two-phase solid-gas flows. Lane *et al.*[4] applied the solution of the gas phase obtained from computational fluid dynamic (CFD) in a two-dimensional axisymmetric formulation and three-dimensional DSMC approaches as an input to a particle trajectory model (PTM) to predict the regolith transport (one-way coupled algorithm).

On the other hand, Liever *et al.*[5] used a hybrid continuum-rarefied solver and combined it with an integrated Lagrangian debris transport tool to solve the Lunar landing problem. Full-scale simulations of Apollo Lunar Excursion Module and Altair landers in 3D space were conducted and plans for direct simulation of erosion and crating process were outlined. He *et al.*[6] extended the previously established framework in the DSMC to include modeling three collisional mechanisms of the molecule-molecule, molecule-particle, and particle-particle. In a more systematic study,[7, 8] a similar approach was applied to investigate the problem in 2D axisymmetric and three-dimensional space setups. To save computational cost, the framework hybridizes the DSMC with DPLR (NASA's continuum flow solver) to solve the continuum region. Li *et al.*[9] analyzed the problem by combining a dynamic method for simulating the solid phase with the DSMC method. Additionally, they applied a microscopic gas-particle two-way coupled method and concluded that their macroscopic approach can provide realistic solutions. Rahimi *et al.*[10] investigated the near-field rocket plume-lunar surface interaction and subsequent surface erosion and regolith dispersal using the classical Navier-Stokes-Fourier (NSF) formulation combined with a discrete phase model (DPM) to estimate the trajectories of the particles. Theoretical models were used as the erosion model to input the particle influx rate to the DPM module. Recently, Chinnappan *et al.*[11] applied a novel coupling technique in the DSMC framework to simulate the Lunar landing problem. In their work, they also applied

an erosion model for providing the influx of particles from the regolith. Another recent work on the DSMC is the simulations of Fontes *et al.*[12], where five different hover altitudes and nine particle sizes were considered. One-way coupled simulations in a steady-state framework were then conducted to derive a numerical correlation for the particle velocity.

The review of literature in this section is limited to those that are dealing with the interaction of a *rarefied gas* with *solid particles*. Various other works, which have solely considered the gas plume impingement[13] or multiphase expanding jets,[14, 15] are available in the literature that were not reviewed here.

In our previous study, we developed a fully continuum-based approach using the discontinuous Galerkin (DG) method.[16] The developed solver in the DG framework was limited to two-dimensional and axisymmetric flows. However, the non-axisymmetric nature of the scour formation necessitates full three-dimensional simulations. The current work is an effort to implement the three-dimensional version of the model equations of our previous study in a computationally less expensive finite volume approach. Furthermore, the strategy in this study includes an unconsolidated layer of dust in the simulation domain rather than applying erosion models that require various ad hoc inputs. Such an approach results in a high-fidelity modeling of the PSI such as what has been conducted by Balakrishnan and Bellan[17]. Compared to the study of Balakrishnan and Bellan[17], which has been conducted for atmospheric conditions, the current formulation benefits from a non-equilibrium gas solver that can be applied for planetary landing situations such as the case in the Lunar landing. Overall, in addition to introducing an efficient continuum framework that covers a wide range of gaseous and solid regimes, the current work adds to the previous literature by presenting a database of three-dimensional simulations that expands upon the physics behind the scour formation and brownout phenomenon in the PSI problem.

As mentioned earlier, although the investigated geometry is axisymmetric, some non-axisymmetric features can be observed on the dusty beds. This counter-intuitive feature was observed in our preliminary studies (**Fig. 2 (a)**) and was also confirmed by the observation on landing sites[18] (**Fig. 2 (b)**) as well as previously published simulations[17] (**Fig. 2 (c)**) and earth-based experiments.[19] The current understanding of the origin of these patterns is the radial expansion of troughs after reaching a stage where owing to the lack of space the initial troughs cannot expand in the circumferential direction anymore. A portion of this study is devoted to

having a deeper look into the governing physics and trying to expand upon this behavior using the vorticity transport equation (VTE) for the first time. Based on this equation, we discuss that in addition to the current explanation based on gas-solid interaction, the vortical structure of the pure gas also contributes to the morphology of the festooned craters.

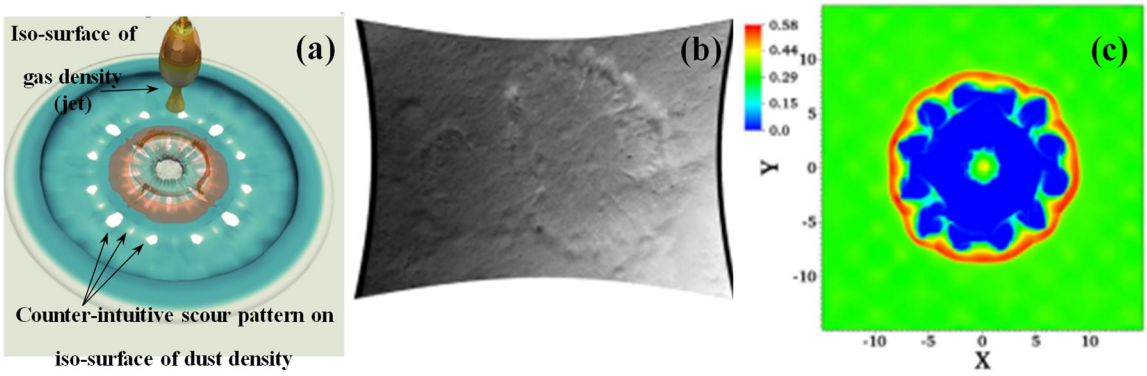

Fig. 2 Counter-intuitive scour formation during landing: (a) Preliminary results of the present study; (b) NASA Mars Science Laboratory (MSL) landing image[18]; (c) Simulation conducted in Jet Propulsion Laboratory (JPL)[17].

Notably, the ambient pressure on Mars allows for the application of the Navier-Stokes equations. However, the very large bulk viscosity of the carbon dioxide gas (which is the dominant species of the Mars atmosphere) is the main challenge for numerical modeling and simulations. Previously, we demonstrated the inability of the first-order theory, even when the Stokes' hypothesis was abandoned (i.e., the Navier-Fourier (NF) model) in such a condition and showed the significant effect of the bulk viscosity on the topology of the solution.[20]

The remainder of this paper is organized as follows. In Sections II mathematical models applied in this work including two-fluid model equations and the corresponding closure models are summarized. Additionally, the derivation of the vorticity transport equation is summarized. In Section III, the applied numerical techniques are summarized. In Section **IV**, after validation of the framework, discussions on pure gas phase simulation results as well as parametric studies in multiphase flow simulations are provided. Finally, conclusions and discussions on the further development of the current study are provided in Section V.

II. MATHEMATICAL MODELING OF RAREFIED AND MULTIPHASE FLOWS IN THE EULERIAN FRAMEWORK

A. Two-fluid model equations for dusty gas flows

A two-fluid model for the simulation of the two-phase solid gas particles was applied. This framework and its derivatives have been applied in our previous works, in both discontinuous Galerkin (the simulation of the interaction of inviscid flow with dust particles,[21] underexpanded jets,[16, 22] flow past prisms at various Mach and Reynolds regimes,[23] and shock-vortex interaction[24]) and finite volume (shock-dust cloud interaction[25]) frameworks. In the aforementioned applications and the current study, the conservation laws (considering viscous effects and solid pressure) can be written as follows:

for the gas phase,

$$\partial_t \mathbf{U}_g + \nabla \cdot \mathbf{F}_g = \mathbf{S} \ , \tag{1}$$

$$\mathbf{U}_g = \begin{bmatrix} \alpha_g \rho_g \\ \alpha_g \rho_g \mathbf{u}_g \\ \alpha_g \rho_g E_g \end{bmatrix}, \quad \mathbf{F}_g = \begin{bmatrix} \alpha_g \rho_g \mathbf{u}_g \\ \alpha_g \rho_g \mathbf{u}_g \mathbf{u}_g + p_g \mathbf{I} + \mathbf{\Pi}_g \\ (\alpha_g \rho_g E_g + p_g)\mathbf{u}_g + \mathbf{\Pi}_g \cdot \mathbf{u}_g + \mathbf{Q}_g \end{bmatrix}, \quad \mathbf{S}_g = \begin{bmatrix} 0 \\ D_{g,s}(\mathbf{u}_s - \mathbf{u}_g) \\ D_{g,s}(\mathbf{u}_s - \mathbf{u}_g) \cdot \mathbf{u}_s + Q_{g,s}(T_s - T_g) \end{bmatrix}, \tag{2}$$

$$E_g = c_v T_g + \frac{1}{2}\left|\mathbf{u}_g\right|^2 \ , \tag{3}$$

and for the solid phase,

$$\partial_t \mathbf{U}_s + \nabla \cdot \mathbf{F}_s = -\mathbf{S} \ , \tag{4}$$

$$\mathbf{U}_s = \begin{bmatrix} \alpha_s \rho_s \\ \alpha_s \rho_s \mathbf{u}_s \\ \alpha_s \rho_s E_s \\ \alpha_s \rho_s e_s \end{bmatrix}, \quad \mathbf{F}_s = \begin{bmatrix} \alpha_s \rho_s \mathbf{u}_s \\ \alpha_s \rho_s \mathbf{u}_s \mathbf{u}_s + p_s \mathbf{I} + \mathbf{\Pi}_s \\ (\alpha_s \rho_s E_s + p_s)\mathbf{u}_s + \mathbf{\Pi}_s \cdot \mathbf{u}_s + \mathbf{Q}_s \\ \alpha_s \rho_s e_s \mathbf{u}_s \end{bmatrix},$$
$$\mathbf{S}_s = \begin{bmatrix} 0 \\ D_{g,s}(\mathbf{u}_s - \mathbf{u}_g) \\ D_{g,s}(\mathbf{u}_s - \mathbf{u}_g) \cdot \mathbf{u}_s + Q_{g,s}(T_s - T_g) \\ \dot{\gamma} \end{bmatrix}, \tag{5}$$

$$E_s = c_m T_p + \frac{1}{2}|\mathbf{u}_s|^2 \ , \tag{6}$$

$$e_s = \frac{3}{2}\Theta \ , \tag{7}$$

$$\alpha_g + \alpha_s = 1, \tag{8}$$

where **U**, **F**, and **S** are the vectors of the conservative variables, fluxes, and source terms, respectively. Variables t, α, ρ, **u**, E, p, T, **Π**, and **Q** represent time, volume fraction, density, velocity vector, total energy, pressure, temperature, viscous stress tensor, and heat flux vector, respectively. In equation (5), $\dot{\gamma}$ is the dissipation of pseudo-thermal energy (PTE) owing to the inelastic particle collisions. Further, D and Q represent the interphase drag and heat flux, respectively. In the Euler-granular model, a new equation for PTE e_s is solved to yield the granular temperature, Θ. The dust density, $\rho_{s,}$ is assumed constant; thus, solid-phase compressibility is controlled by the changes in the solid volume fraction. Various types of constitutive relationships for equation (5) are available in the literature (see Refs. [26-29]). This study assumes that the flow is dilute; hence, a pressureless Euler type of equation is applied for the simulations.

B. Second-order Boltzmann-Curtiss-based hydrodynamics model for modeling gas in thermal non-equilibrium using the method of moments

1. Conservation laws from the Boltzmann-Curtiss kinetic equation

Because of the collisional invariant properties of mass, momentum, and energy, the exact conservation laws can be derived from the Boltzmann-Curtiss kinetic transport equation. The Boltzmann-Curtiss kinetic equation for diatomic (and linear polyatomic) molecules with a moment of inertia, I_m and an angular momentum, **j**, can be expressed [30] as follows:

$$\left(\frac{\partial}{\partial t}+\mathbf{v}\cdot\nabla+\frac{j}{I_m}\frac{\partial}{\partial\psi}+F\cdot\nabla_v\right)f\left(\mathbf{v},\mathbf{r},\mathbf{j},\psi,t\right)=C\left[f\right], \tag{9}$$

where $f,\mathbf{v},\mathbf{r},\psi,j$, and $C[f]$ represent the distribution function, particle velocity, particle position, azimuthal angle associated with the orientation of the particle, magnitude of the angular momentum vector **j**, and collision integral, respectively. F is the external force on the unit mass and ∇_v denotes the gradient vector in the velocity space. The Boltzmann-Curtiss kinetic equation describes the changes in the probability distribution function along a molecular pathway owing to intermolecular collisions and under the presence of F.

The conservation laws of mass, momentum, and total energy for monatomic gases can be derived directly from the Boltzmann-Curtiss kinetic equation by noting that the molecular expressions for conserved variables are collision invariants. After differentiating the statistical definition of the conserved variables with time and combining them with the Boltzmann-Curtiss kinetic equation, the following conservation laws, all of which are an exact consequence of the Boltzmann-Curtiss kinetic equation, can be derived [31-33]:

In the absence of F,

$$\frac{\partial}{\partial t}\begin{bmatrix}\rho\\ \rho\mathbf{u}\\ \rho E\end{bmatrix}+\nabla\cdot\begin{bmatrix}\rho\mathbf{u}\\ \rho\mathbf{u}\mathbf{u}+p\mathbf{I}\\ \left(\rho E+p\right)\mathbf{u}\end{bmatrix}+\nabla\cdot\begin{bmatrix}0\\ \Pi+\Delta\mathbf{I}\\ \left(\Pi+\Delta\mathbf{I}\right)\cdot\mathbf{u}+\mathbf{Q}\end{bmatrix}=0. \tag{10}$$

There are two different sets of macroscopic variables; the conserved $\left(\rho, \rho\mathbf{u}, \rho E\right)$ and non-conserved $\left(\boldsymbol{\Pi}, \Delta, \mathbf{Q}\right)$ variables, where $\mathbf{u}$ is the bulk velocity vector; E is the total energy density; $\boldsymbol{\Pi}, \Delta, \mathbf{Q}$ represent the shear stress tensor, excess normal stress, and heat flux, respectively. Notably, the set of equations (10) remain open unless the non-conserved variables are determined. Because of the presence of non-conserved variables $\boldsymbol{\Pi}, \Delta, \mathbf{Q}$ (whose molecular definitions do not yield a collisional invariant), the evolution equations of these variables should be derived.

2. Boltzmann-Curtiss-based constitutive relationships for the gas phase

The same approach used to derive the conservation laws can be applied to the derivation of the evolution equation of the non-conserved variables. After differentiating the statistical definition of the corresponding non-conserved variables with time and combining them with the Boltzmann-Curtiss kinetic equation, the following first-order Boltzmann-Curtiss-based constitutive model of the shear stress tensor, the excess normal stress, and heat flux vector can be derived:

$$\begin{aligned} \boldsymbol{\Pi}_g &= -2\mu_g \left[\nabla \mathbf{u}_g\right]^{(2)}, \\ \boldsymbol{\Delta}_g &= -\mu_b \nabla \cdot \mathbf{u}_g, \\ \mathbf{Q}_g &= -\kappa_g \nabla T_g. \end{aligned} \tag{11}$$

The symbol $\left[\mathbf{A}\right]^{(2)}$ denotes the traceless symmetric part of the second-rank tensor $\mathbf{A}$. These first-order linear relations were obtained after very crude first-order approximations; all kinematic terms except for the thermodynamic force term were neglected in the evolution equations and the collision-related dissipation terms were linearized. Moreover, a distinction should be made regarding the NF and NSF relations. In the latter, Stokes' hypothesis, $\mu_b = 0$, was applied.

Similarly, the second-order Boltzmann-Curtiss-based constitutive models can be derived by first differentiating the statistical definition of the non-conserved variables with time and then combining them with the Boltzmann-Curtiss kinetic equation. Once the two tenets—Eu's cumulant expansion based on the canonical distribution function in the exponential form to the

explicit calculation of the dissipation term,[34, 35] and Myong's closing-last balanced closure [33]— are applied to the evolution equations and after introducing the so-called adiabatic approximation derived from the observation that the relaxation times of the non-conserved variables are very short, being on the order of 10^{-10} second, the following second-order constitutive model can be derived from the Boltzmann-Curtiss kinetic equation: [31-33]

$$\begin{aligned}
&\hat{\mathbf{\Pi}} q_{2nd}\left(c\hat{R}\right) = \left(1+f_b\hat{\Delta}\right)\hat{\mathbf{\Pi}}_0 + \left[\hat{\mathbf{\Pi}}\cdot\nabla\hat{\mathbf{u}}\right]^{(2)} \\
&\hat{\Delta} q_{2nd}\left(c\hat{R}\right) = \hat{\Delta}_0 + \frac{3}{2}\left(\hat{\mathbf{\Pi}} + f_b\hat{\Delta}\mathbf{I}\right):\nabla\hat{\mathbf{u}} \\
&\hat{\mathbf{Q}} q_{2nd}\left(c\hat{R}\right) = \left(1+f_b\hat{\Delta}\right)\hat{\mathbf{Q}}_0 + \hat{\mathbf{\Pi}}\cdot\hat{\mathbf{Q}}_0 \qquad (12) \\
&\text{where } q_{2nd}\left(c\hat{R}\right) = \frac{\sinh(c\hat{R})}{c\hat{R}}, \quad \hat{R}^2 \equiv \hat{\mathbf{\Pi}}:\hat{\mathbf{\Pi}} + (5-3\gamma) f_b\hat{\Delta}^2 + \hat{\mathbf{Q}}\cdot\hat{\mathbf{Q}}.
\end{aligned}$$

The caret (ˆ) over a symbol represents a quantity with the dimension of the ratio of the stress to the pressure. The values of $\mathbf{\Pi}_0$, Δ_0, and $\mathbf{Q}_0$ are determined by the Newtonian law of shear and bulk viscosity, as well as the Fourier law of heat conduction. $\hat{R}$ represents the Rayleigh–Onsager dissipation function,[36] and constant c has a value between 1.0138 (Maxwellian) and 1.2232; for instance, 1.018 for the nitrogen gas molecule.[31-33] The Rayleigh-Onsager dissipation function gives a direct measure of departure from equilibrium. The first-order cumulant approximation for the nonlinear factor '$q_{2nd}\left(c\hat{R}\right)$' in (12) describes the mode of energy dissipation accompanying the irreversible processes and is directly related to the nonequilibrium entropy production in the system.[37] The factor $f_b = \mu_b/\mu$ is the ratio of the bulk viscosity to the shear viscosity. Its value may be experimentally determined using a sound wave absorption measurement; for instance, 0.8 for the nitrogen gas molecule. Although the second-order constitutive model (12) involves highly nonlinear implicit algebraic equations, they can be easily solved numerically for the given thermodynamic driving forces, based on the concept of decomposition and the method of iteration.[31-33] More details regarding the second-order Boltzmann-based and Boltzmann-Curtiss-based constitutive relationships and the closing-last balanced closure can be found in [31, 33, 38, 39].

C. Analysis of vorticity growth rates in the two-phase jet impingement problem

The vorticity growth rates in the multiphase jet impingement problem were also analyzed. The well-known vorticity transport equation for inviscid compressible flow is given as

$$\frac{D\boldsymbol{\omega}}{Dt} = (\boldsymbol{\omega}\cdot\nabla)\mathbf{u} - \boldsymbol{\omega}(\nabla\cdot\mathbf{u}) + \frac{1}{\rho^2}\nabla\rho\times\nabla p\,. \tag{13}$$

Recently a new vorticity transport equation that includes viscous terms and abandons Stokes' hypothesis has been derived for diatomic and polyatomic gases.[40] Based on this derivation, the VTE of the NF equation for gas (or solid) in a two-phase flow can be easily derived. The momentum equation is given as

$$\frac{\partial\mathbf{u}}{\partial t} = -(\mathbf{u}\cdot\nabla)\mathbf{u} - \frac{1}{\hat{\rho}}\nabla p + \frac{1}{\hat{\rho}}\nabla\cdot\left[\mu\left(2\left[\nabla\mathbf{u}\right]^{(2)} + f_b(\nabla\cdot\mathbf{u})\mathbf{I}\right)\right] + \frac{D}{\hat{\rho}}(\mathbf{u}_S - \mathbf{u}) \tag{14}$$

where $\hat{\rho}\equiv\alpha\rho$. This will yield

$$\begin{aligned}\frac{D\boldsymbol{\omega}}{Dt} &= (\boldsymbol{\omega}\cdot\nabla)\mathbf{u} - \boldsymbol{\omega}(\nabla\cdot\mathbf{u}) + \frac{\mu}{\hat{\rho}}\nabla^2\boldsymbol{\omega}\\ &+\frac{1}{\hat{\rho}^2}\nabla\hat{\rho}\times\nabla p - \frac{\mu}{\hat{\rho}^2}\nabla\hat{\rho}\times\nabla^2\mathbf{u} - \left(\frac{1}{3}+f_b\right)\frac{\mu}{\hat{\rho}^2}\nabla\hat{\rho}\times\nabla(\nabla\cdot\mathbf{u})\\ &+\frac{1}{\hat{\rho}}(\nabla\mu\cdot\nabla)\boldsymbol{\omega} + \frac{1}{\hat{\rho}}(\boldsymbol{\omega}\cdot\nabla)\nabla\mu - \frac{\boldsymbol{\omega}}{\hat{\rho}}\nabla^2\mu + \frac{1}{\hat{\rho}}\nabla\mu\times\nabla^2\mathbf{u} + \frac{2}{\hat{\rho}}\nabla(\nabla\mu\cdot\nabla)\times\mathbf{u}\\ &-\frac{1}{\hat{\rho}^2}\nabla\hat{\rho}\times(\nabla\mu\times\boldsymbol{\omega}) - \frac{2}{\hat{\rho}^2}\nabla\hat{\rho}\times(\nabla\mu\cdot\nabla)\mathbf{u} + \left(\frac{2}{3}-f_b\right)\frac{(\nabla\cdot\mathbf{u})}{\hat{\rho}^2}\nabla\hat{\rho}\times\nabla\mu\\ &+\frac{1}{\hat{\rho}}\nabla\mu\times\nabla(\nabla\cdot\mathbf{u}) + \frac{D}{\hat{\rho}}(\nabla\times\mathbf{u}_S - \boldsymbol{\omega}) + \nabla\left(\frac{D}{\hat{\rho}}\right)\times(\mathbf{u}_S - \mathbf{u}).\end{aligned} \tag{15}$$

The corresponding equation for nonlinear-coupled constitutive relationship (NCCR) can be calculated as follows:

$$\frac{D\boldsymbol{\omega}}{Dt}=\left(\boldsymbol{\omega}\cdot\nabla\right)\mathbf{u}-\boldsymbol{\omega}\left(\nabla\cdot\mathbf{u}\right)+\frac{1}{\hat{\rho}^2}\nabla\hat{\rho}\times\nabla p-\nabla\times\left(\frac{\mathbf{\Pi}}{\hat{\rho}}\right)+\frac{D}{\hat{\rho}}\left(\nabla\times\mathbf{u}_S-\boldsymbol{\omega}\right)$$
$$+\nabla\left(\frac{D}{\hat{\rho}}\right)\times\left(\mathbf{u}_S-\mathbf{u}\right). \tag{16}$$

Note that the stress term in NCCR cannot be further simplified, as it is not a linear function of the velocity gradient. For a comprehensive derivation of the above relations, see the appendix of Ejtehadi*, et al.*[20].

The terms in the right-hand side of equation (16) from right to left include the stretching term (which is the lengthening of vortices in a three-dimensional fluid flow, and it associated with a corresponding increase in the vorticity component in the stretching direction), which is an important mechanism in the dynamics of turbulence; dilatation term (responsible for the fluid convection and thermal expansion, which remains important in highly compressible fluids); the baroclinicity term (a measure of how misaligned the gradient of pressure is from the gradient of density in a fluid), which is responsible for the production of small-scale rolled up vortices at different density interfaces; viscous term (owing to presence of viscosity). The last two terms are known as multiphase terms (owing to the presence of a relative velocity between the two phases).

III. NUMERICAL MODELING, VERIFICATION, AND VALIDATION

A coupled density-based solver was developed to solve the system of equations discussed in the previous section. The advective terms are discretized using the hybrid HLLC-AUSM method of Koop[41] equipped with the flux limiter of Barth and Jespersen[42] to avoid spurious oscillations near discontinuities. After the application of the method of lines to decouple spatial and temporal discretizations, an explicit time integration method (a low-storage fourth-order Runge-Kutta scheme) is applied for solving the semi-discrete equations.

In this study, a simple yet effective strategy with the basic idea of adding and subtracting a pressure-related term to the momentum and energy equations of the dust phase is applied. Although this manipulation does not have any algebraic consequences, from a numerical point of view, the new system has a significant advantage, recovering the strict hyperbolicity of the

equation. The equation of the dust phase (in the Euler-Euler model) after the addition and subtraction of a pressure-related term can be written as follows:

$$\partial_t \begin{bmatrix} \alpha_s \rho_s \\ \alpha_s \rho_s \mathbf{u}_s \\ \alpha_s \rho_s E_s \end{bmatrix} + \nabla \cdot \begin{bmatrix} \alpha_s \rho_s \mathbf{u}_s \\ \alpha_s \rho_s \mathbf{u}_s \mathbf{u}_s + p_s \mathbf{I} - p_s \mathbf{I} \\ (\alpha_s \rho_s E_s + p_s - p_s)\mathbf{u}_s \end{bmatrix} = -\mathbf{S}. \tag{17}$$

Equivalently in split form, it can be written as

$$\partial_t \begin{bmatrix} \alpha_s \rho_s \\ \alpha_s \rho_s \mathbf{u}_s \\ \alpha_s \rho_s E_s \end{bmatrix} + \nabla \cdot \begin{bmatrix} \alpha_s \rho_s \mathbf{u}_s \\ \alpha_s \rho_s \mathbf{u}_s \mathbf{u}_s + p_s \mathbf{I} \\ (\alpha_s \rho_s E_s + p_s)\mathbf{u}_s \end{bmatrix} = \nabla \cdot \begin{bmatrix} 0 \\ p_s \mathbf{I} \\ p_s \mathbf{u}_s \end{bmatrix} - \mathbf{S} \tag{18}$$

In this equation, the inviscid flux is equivalent to that of the Euler equation of the gas phase. Thus, the conservation law can be considered strictly hyperbolic, and the additional term on the right-hand side can be handled in a similar way that the source terms are treated. The idea is inspired by the strategy that was developed initially in computational magnetohydrodynamics[43-45] and has been applied in other fields, including aircraft icing.[46] The approach is tested for the two-fluid equation model of dusty gases in a modal discontinuous Galerkin framework,[16, 24] as well as finite volume framework.[20, 25]

A. Problem definition

The problem undertaken is a 3D nozzle jet gas flow impinging onto a surface at near-vacuum that represents the descent phase of a lunar landing. The surface is covered with a blanket of dust that represents the lunar regolith. The nozzle configuration is similar to that of the Apollo descent module.[8] To save computational cost, a quarter of the domain is simulated. A schematic of the problem, defining the boundary conditions, domain size, and a sample grid is shown in **Fig. 3**.

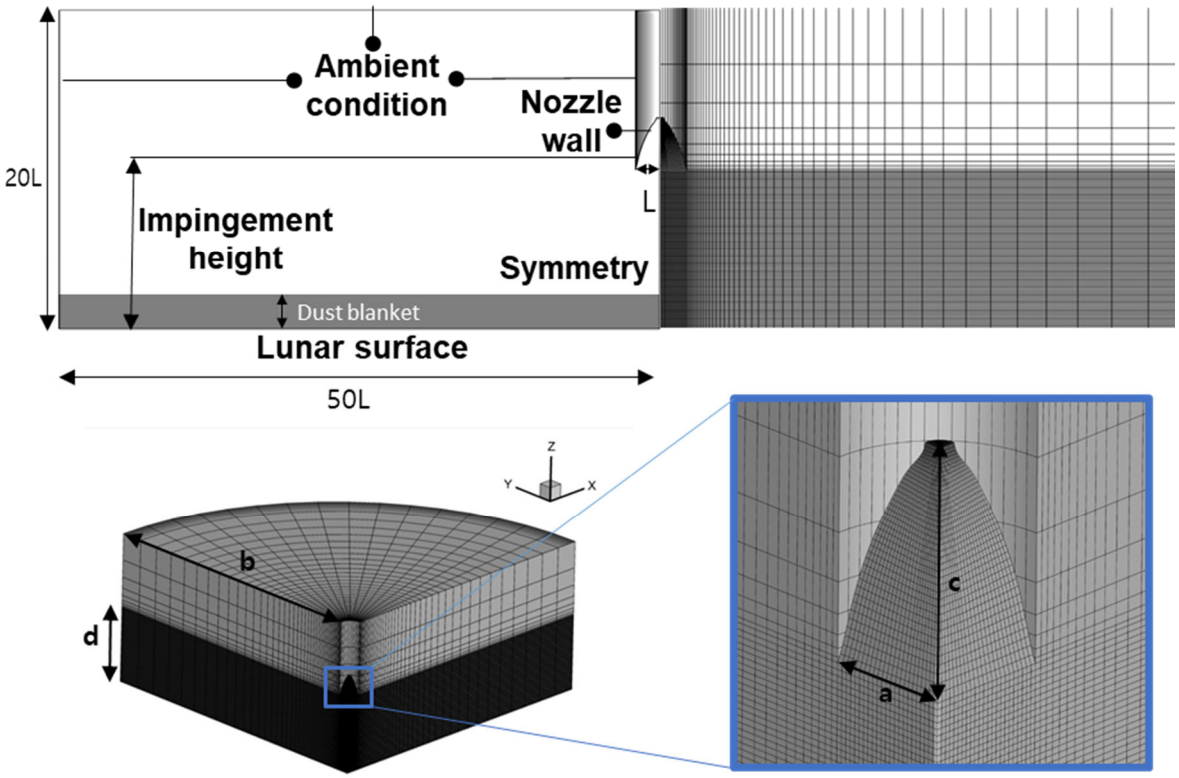

Fig. 3 Schematic of the problem, boundary conditions, and a sample grid.

The major exhaust products of the Titan stage 2 engine were H_2O, NH_3, CO, NO, O_2, CO_2, and NO_2. In this study, a calorically perfect gas with properties identical to H_2O was simulated to be consistent with the studies of Morris, *et al.*[8]. The estimated values of specific heat ratio, gas constant, and molar weight are 1.3, 461.5 J/kgK, and 18.02 kg/kmol, respectively. Sutherland's law, details of which are provided in the following sections, is applied as the viscosity model. The throat condition is also set to be consistent with Morris, *et al.*[8], which results in an average Mach number of 5 at the nozzle exit. Notably, the real gas effects were not considered in this study. Such effects besides the geometry of the nozzle play a major function in determining the structure of the underexpanded jet and features such as the reflection point, shock standoff distance, and nozzle exit average values. However, we have set these parameters in such a way that these features are consistent with the simulations of Morris, *et al.*[8].

B. Verification and validation

A systematic grid study has been conducted to ensure that the solutions are grid-independent. Therefore, grids with four different resolutions in both axial and radial directions were generated and run. Number of divisions of each section of the grid and overall mesh count are summarized in **Table 1**.

Table 1 Details of different meshes used in grid independence study (**a**, **b**, **c**, and **d** are marked on **Fig. 3**).

Grid	**a**	**b**	**c**	**d**	Overall mesh count
1	15	45	10	30	40,960
2			20	60	74,720
3			40	120	142,240
4			80	240	277,280
5	8	20	40	120	72,320
6	15	45			142,240
7	25	90			399,840
8	40	120			744,960

Fig. 4 demonstrates the solution of the pressure for different grids. For the analysis in the axial direction, the pressure profile on the symmetry axis is plotted (grids 1 to 4 in **Table 1**), whereas in the radial direction two cross-sections (nozzle exit and lunar surface) are used (grids 5 to 8 in **Table 1**). As can be observed, grids 3 and 4 in **Fig. 4 (a)** and grids 7 and 8 in **Fig. 4 (b)** and **(c)** provide almost identical results in each direction and hence, grid 7 which satisfies the requirement for both directions is used for the rest of analysis in this study.

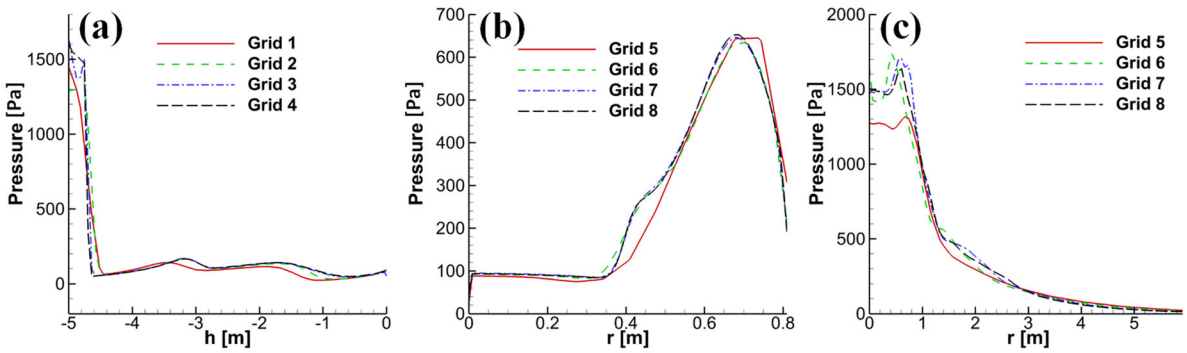

Fig. 4 Grid independence analysis: pressure distribution on (a) axis of symmetry; (b) nozzle exit; (c) impingement surface.

Even though the NCCR model is tested and validated in different other contents,[33, 39, 47-50] a validation test case specific to the problem at hand is provided. **Fig. 5** demonstrates a comparison of the pressure solution of the developed solver with the work of Morris, *et al.*[8] at the hover altitude of 5 m. As can be observed, the overall features of the flow are consistent. Some discrepancies are also observed, which could be owing to real gas effects or slightly different profiles of the nozzle. However, the differences are minute, meaning features such as the location of the reflection point, shock standoff distance, and qualitative structure of the flow are consistent with the reference work.

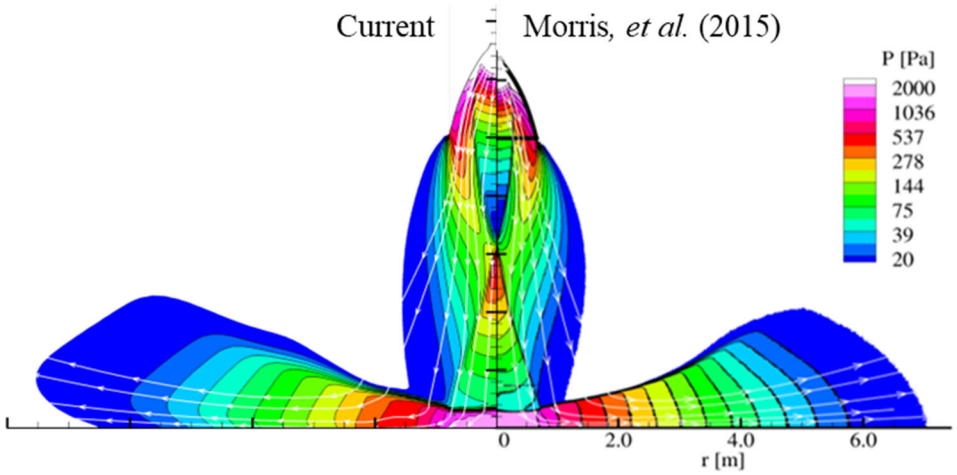

Fig. 5 Comparison of the NCCR solution of the pressure and streamlines with the DSMC solution of Morris, *et al.*[8] at a hovering altitude of 5 m.

As discussed in Ref.[10], the near-field plume can be almost correctly predicted by the linear NSF theory. However, in special conditions, deviation in the models can be significant. To demonstrate this fact, a test case is simulated. **Fig. 6** shows the density isosurfaces colored by the Rayleigh–Onsager number (that is, a Rayleigh–Onsager dissipation function in a non-dimensional form) for two different cases. In both cases, the ambient pressure is set to near-vacuum condition (p_{amb} = 0.1 Pa). **Fig. 6** (a) and (b) represent the case where the inlet pressure p_{in} is set to 100 Pa (a pressure ratio of 1000), whereas **Fig. 6** (c) and (d) correspond to an inlet pressure of 10 Pa (a pressure ratio of 100). The NSF and NCCR solvers are used to solve both scenarios. The NSF solution under-predicts the location of the reflected shock (consequently, the SS position). The gap between the two models is even greater when the inlet pressure is reduced (an increase in rarefaction effects). The other features affected by this variation include

the shock standoff curvature, degree of the plume expansion, and diffusion of the discontinuities owing to viscous domination.

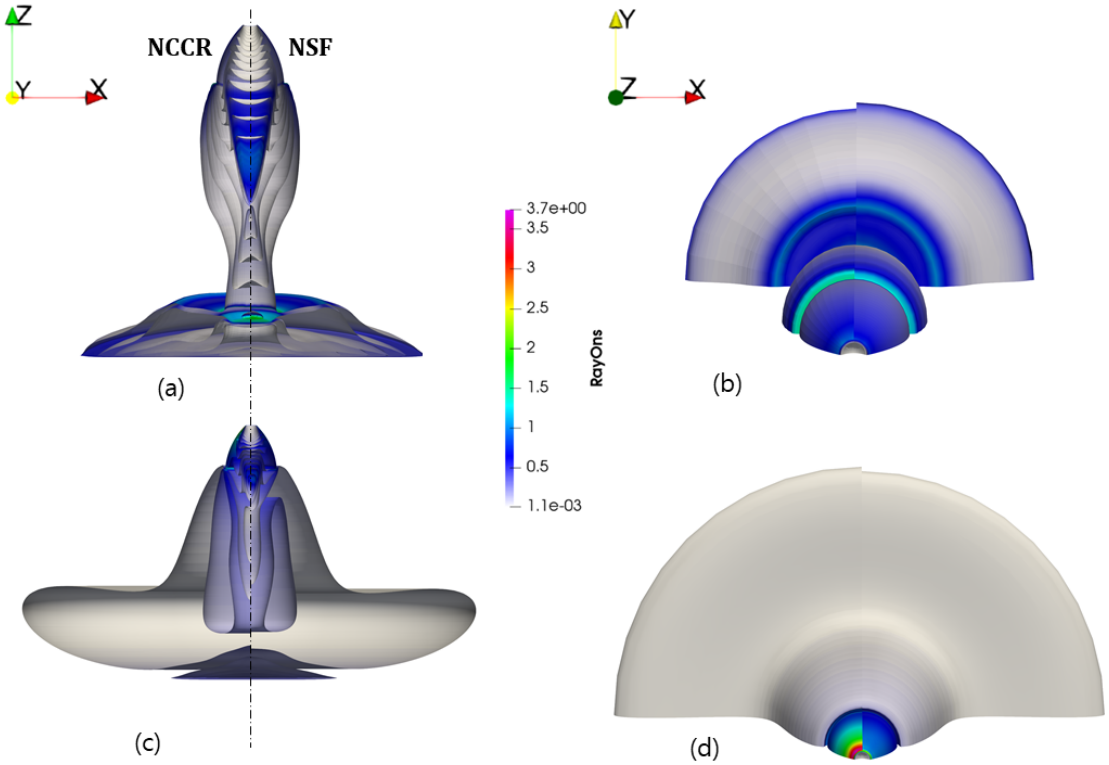

Fig. 6 Density isosurfaces colored by the Rayleigh–Onsager number: (a) and (b) at p_{in} = 100 Pa and pressure ratio = 1000; (c) and (d) at p_{in} = 10 Pa and pressure ratio = 100.

IV. RESULTS AND DISCUSSIONS

A. Pure gas (single-phase) analysis.

Before delving into multiphase analysis, the effects of variation of some of the parameters on the structure of the plume including ambient pressure, gas dynamic viscosity, and bulk viscosity were investigated. Although other variables can affect the structure of the plume too (e.g., pressure ratio, working gas, geometrical features such as nozzle contour as well as expansion ratio and the impingement height), we limit our investigation only to the selected parameters for which it is not easy to find data in the literature. We analyze both the transient and steady phases of the flow by plotting contours on the symmetry plane as well as isosurfaces of the terms in the vorticity transport equation to highlight the counterintuitive behaviors. A summary of the single-phase test cases is provided in **Table 2**.

Table 2 Pure gas test cases.

Test case	Ambient pressure [Pa]	Viscosity (μ_0) [N.s/m^2]	f_b	Inlet Temperature [K]	Inlet pressure [Pa]
1	5	0.00005	1	3000	144630
2	20	0.00005	1	3000	144630
3	100	0.00005	1	3000	144630
4	5	0.0001	1	3000	144630
5	5	0.001	1	3000	144630
6	5	0.00005	0	3000	144630
7	5	0.00005	2	3000	144630
8*	5	0.00005	1	3000	14463
9*	5	0.00005	1	5000	144630
10*	5	0.00005	1	3000	144630
11*	5	0.00005	1	1000	144630

* Simulations on the super-fine grid for investigation of vorticity growth rates.

1. Back pressure

Fig. 7 demonstrates the effect of the variation of ambient pressure on the structure of the flowfield. The contours present the pressure solution for simulations with three different background pressures (cases 1 to 3: p_{amb} = 5, 10, and 100 pa) on the symmetry plane. The development of the plume in axial and radial directions using reference lines (dashed lines) marking the jet front (JF) is shown in **Fig. 7 (a)** and **(b)**. As observed in the figure, in lower pressure ambient the flow is developed faster in both axial and radial directions. In **Fig. 7 (c)**, where the reflection has been developed for all three cases, it can be observed that the ambient pressure does not affect the location of the reflection point (RP). However, this parameter can effectively change the location of the standoff shock (SS), as shown in **Fig. 7 (b)** and **(c)**. This is because the location of the reflection point is determined by the reflection of the expansion waves which itself is largely dependent on the nozzle contour as well as the thermophysical properties of the gas while the shock standoff distance is mainly determined by the strength of

the shock wave, on top of the aforementioned parameters. Hence, the nozzle total pressure to the ambient pressure plays a critical role in the distance where this normal shock stands.

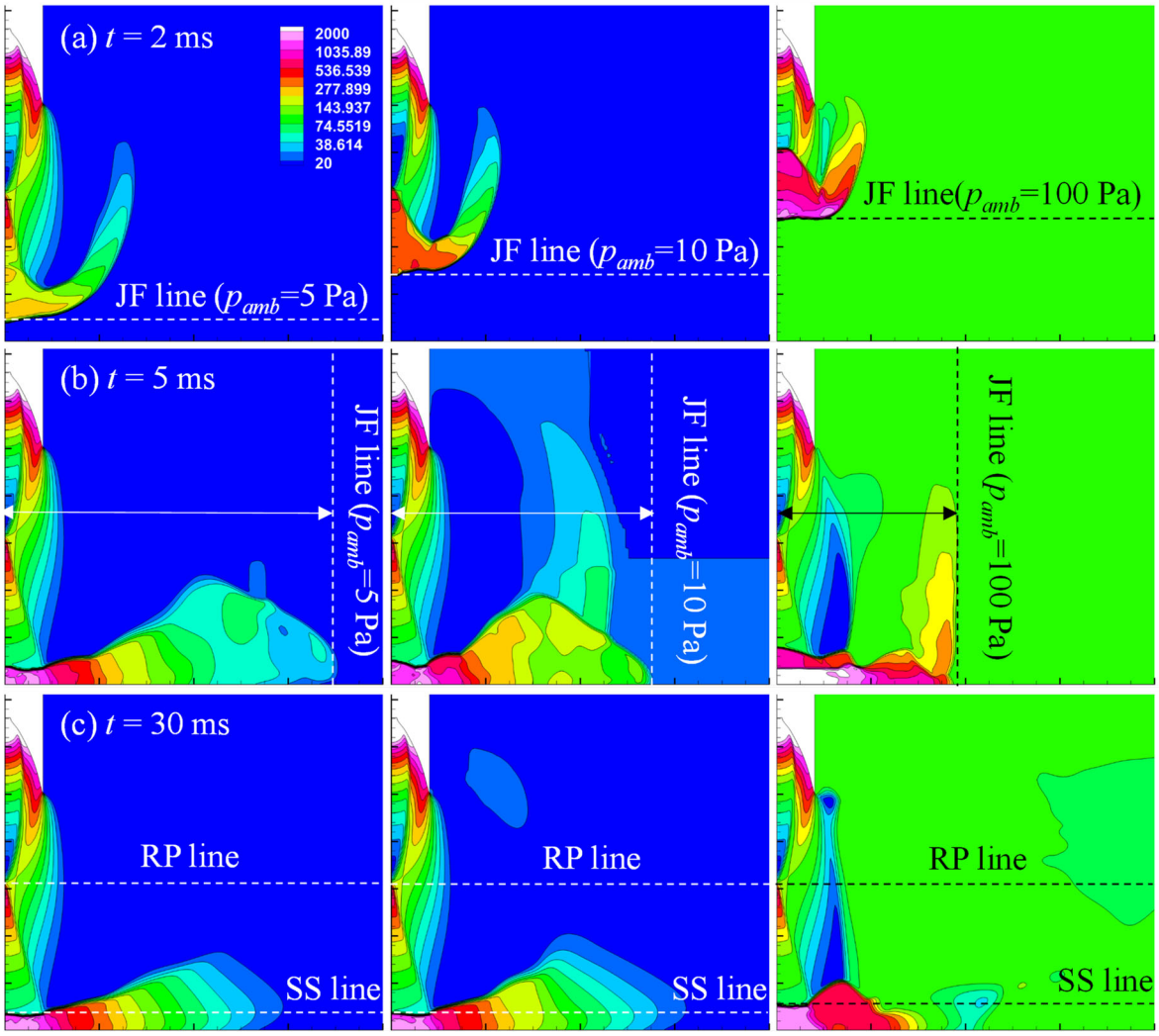

Fig. 7 Effects of variation of the ambient pressure on the structure of the plume (pressure contours) at (a) t = 2 ms; (b) t = 5 ms; (c) t = 30 ms (Left column, case 1: p_{amb} = 5 Pa; middle column, case 2: p_{amb} = 10 Pa; right column, case 3: p_{amb} = 100 Pa) JF: Jet Front, RP: Reflection Point, SS: Standoff Shock.

Fig. 8 shows the effects of ambient pressure variation on the axial symmetry line and at a specific time in a more quantitative manner. In this figure, both pressure and temperature distribution o the axis of symmetry are plotted against the hover altitude (h). Heights h = 0 and -5 m correspond to the nozzle exit plane and the impingement surface, respectively. As the figure illustrates, such variation does not affect the RP but can significantly affect the location of the SS when the ambient pressure variation is large. In these plots, as the altitude decreases both the pressure and temperature decrease, followed by a sudden jump at h = 2 m which marks

the location of the reflection point. All three profiles which represent different ambient pressure cases are overlapped at this point. With a further decrease of the altitude, pressure, and temperature values continue to decline at an identical rate to the rate of decrease before the reflection point. The next jump in the profiles represents the location of the standoff shock. Here the deviation between the 100 Pa case with 5 and 10 Pa cases is obvious specifically in the temperature profile.

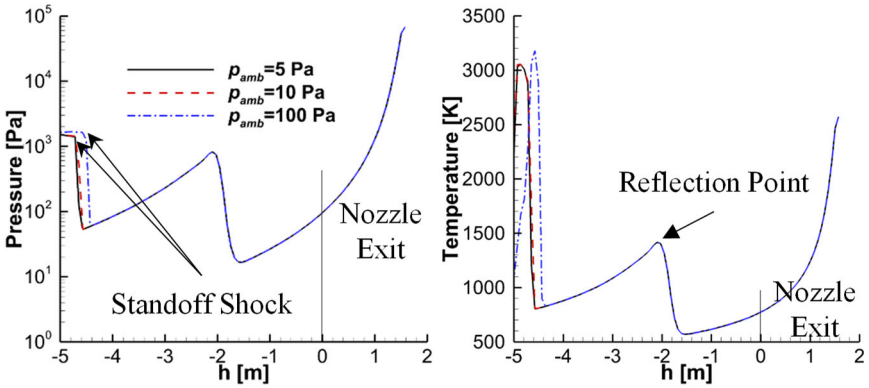

Fig. 8 Effects of variation of the ambient pressure (t = 30 ms). p_{amb} = 5, 10, and 100 pa correspond to cases 1 to 3, respectively.

2. Gas viscosity

As mentioned earlier, the Sutherland's model of viscosity is applied in the current study

$$\frac{\mu}{\mu_0} = \left(\frac{T}{T_0}\right)^{3/2} \frac{T_0 + S_\mu}{T + S_\mu}, \tag{19}$$

where μ_0, T_0, and S_μ are the reference viscosity, temperature, and Sutherland constant, respectively. In **Fig. 9**, viscosity (top) and pressure contours (bottom) are analyzed for three different cases. In the simulations of **Fig. 9**, T_0 and S_μ are set to 350 and 1024 K, respectively, and μ_0 is varied between 0.00001 to 0.0001 N.s/m^2 (cases 1, 4, and 5) to check the effect of viscosity on the structure of the plume. It was observed that the dynamic viscosity variation remarkably affects the structure of the plume. An increase in the viscosity value leads to upstream movement of the RP and SS. For smaller values, the region between the surface and the SS becomes unstable, leading to shock wave oscillation. These instabilities, which originate

from the shear layer starting from the exit plane, are convected towards the surface and they form a feedback loop and are towards the farfield region (**Fig. 9 (a)**).

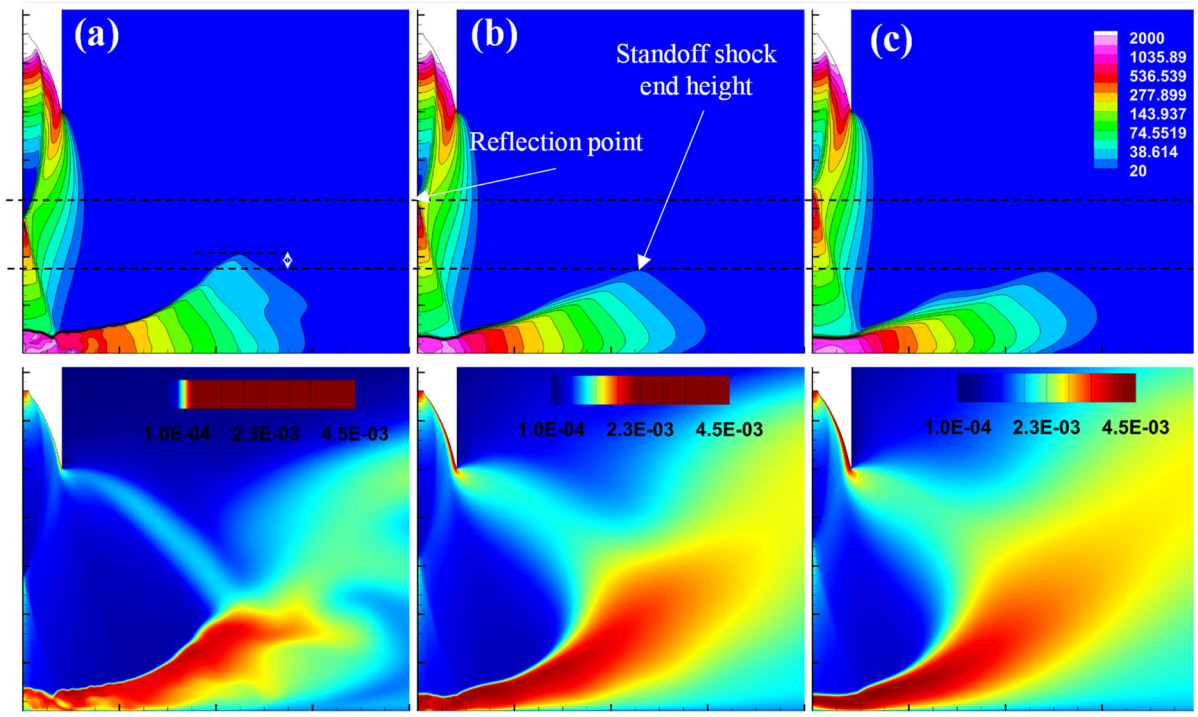

Fig. 9 Effects of variation of the dynamic viscosity on the structure of the plume: pressure (top) and viscosity contours (bottom) at $t = 0.02$ s: (a) case 1: $\mu_0 = 0.00001$ Pa.s; (b) case 4: $\mu_0 = 0.00005$ Pa.s; (c) case 5: $\mu_0 = 0.0005$ Pa.s.

3. Bulk viscosity

Fig. 10 illustrates the effect of bulk viscosity on the structure of the plume (cases 1, 6, and, 7). The trends remain almost identical with the variation of the dynamics viscosity. The significant difference is that in the investigated range, the RP is less affected (compared to the variation observed in the parametric analysis of dynamic viscosity); however, the curvature of the SS decreases as the bulk viscosity increases, as shown in **Fig. 10 (a)** to **(c)**. In **Fig. 10 (d)** and **(e)**, plots of pressure and temperature are provided to demonstrate how the bulk viscosity variation can affect the location of the standoff shock and the reflection point. These figures also confirm the visual observation in contours of **Fig. 10 (a)** to **(c)**, i.e., an almost negligible effect of bulk viscosity on either the RP or SS locations.

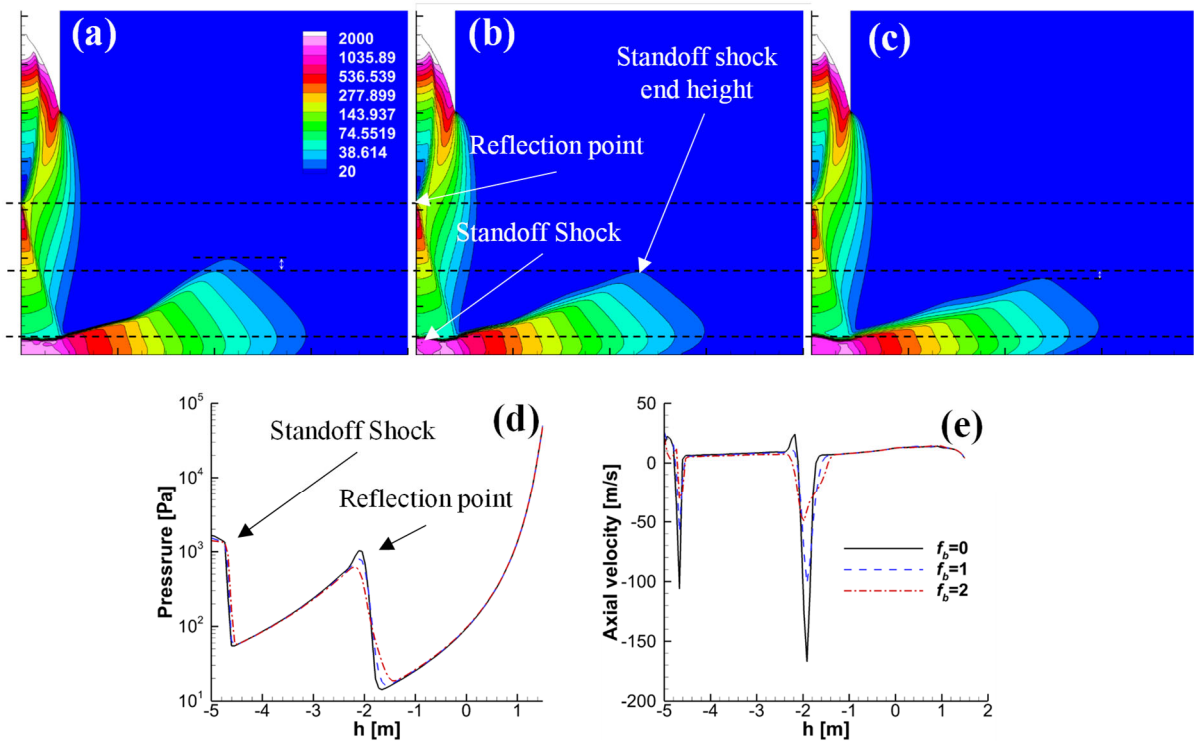

Fig. 10 Effects of variation of the bulk viscosity: pressure contours for (a) case 1: $f_b = 0$; (b) case 6: $f_b = 1$; (c) case 7: $f_b = 2$; and distribution of (d) pressure; (e) axial velocity on the axis of symmetry.

4. Vorticity growth rates and counterintuitive patterns

To investigate the counter-intuitive patterns discussed in **Fig. 2**, the terms in the vorticity transport equation are calculated separately. Compare to the standard grid used in the rest of the simulations, for the cases of this section, the computational domain is halved in the radial direction and the number of divisions in both radial and axial directions is proportionally increased resulting in a super-fine grid with more than 10 million elements in the vicinity of the nozzle. First, a snapshot of the vorticity contour at $t = 0.01$ s and a height of 0.6 m from the surface is plotted for cases 8 to 11 of **Table 2**. The decrease in the inlet temperature is equivalent to an increase in the global Mach and a decrease in Kn numbers. **Fig. 11 (a)** and **(b)** represent the cases where the flow patterns are either very smooth or chaotic. Therefore, the possibility of observing non-axisymmetric patterns is low in these cases. However, cases 9 and 10 show patterns that are consistent with the counterintuitive patterns that we are interested.

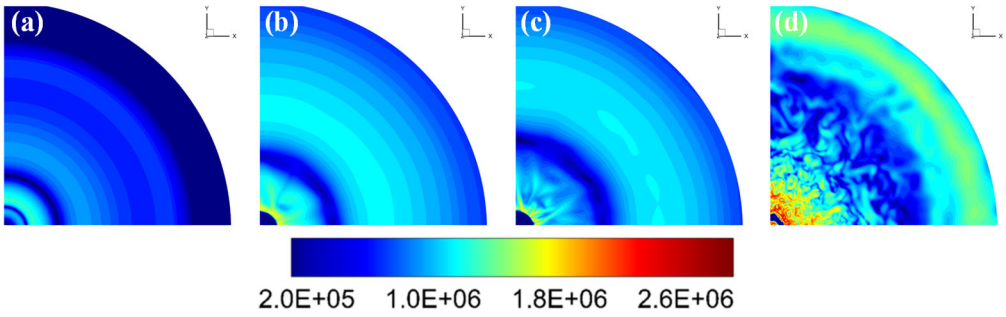

Fig. 11 Vorticity magnitude snapshots at t = 0.01 s and a height of 0.6 m from the surface for superfine grid: (a) case 8; (b) case 9; (c) case 10; (d) case 11.

Fig. 12 represents the spatial integration of the following terms:

$$\left|\boldsymbol{\omega}_{stretching}\right|(t)=\int_D\left|(\boldsymbol{\omega}\cdot\nabla)\mathbf{u}\right|dxdy\,, \tag{20}$$

$$\left|\boldsymbol{\omega}_{dilatation}\right|(t)=-\int_D\left|\boldsymbol{\omega}(\nabla\cdot\mathbf{u})\right|dxdy\,, \tag{21}$$

$$\left|\boldsymbol{\omega}_{baroclinicity}\right|(t)=\int_D\left|\frac{1}{\hat{\rho}^2}\nabla\hat{\rho}\times\nabla p\right|dxdy\,, \tag{22}$$

$$\left|\boldsymbol{\omega}_{viscous}\right|(t)=\int_D\left|\nabla\times\left(\frac{\boldsymbol{\Pi}}{\hat{\rho}}\right)\right|dxdy\,. \tag{23}$$

Here, D represents the integration domain (i.e., the entire computational domain). As shown in **Fig. 12**, the viscous term has a significant overall contribution compared to the other terms. However, this is not sufficient to conclude that the viscous term is responsible for nonaxisymmetric behavior. It can be observed that with the increase of the Mach number, the contribution of the viscous term drastically reduces; however, the contribution of other terms slightly increases, as shown from **Fig. 12 (b)** to **(c)**. Among all the investigated cases, the contribution of the viscous term is highest for case 9 (**Fig. 12 (b)**), which is the case where the nonaxisymmetric patterns are more highlighted.

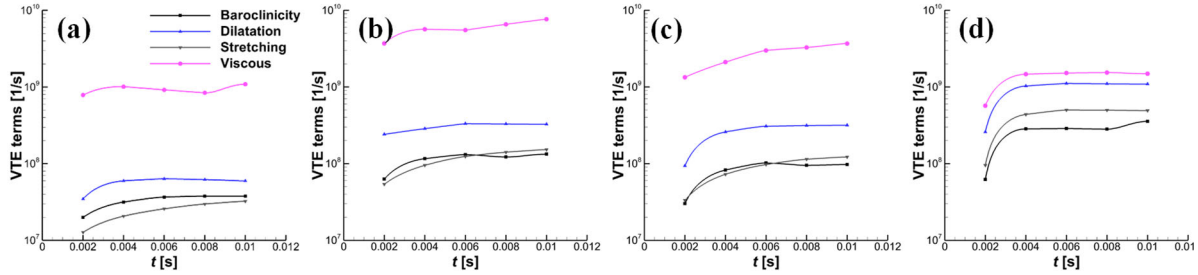

Fig. 12 Time evolution of different terms in the viscosity transport equation for different cases: (a) case 8; (b) case 9; (c) case 10; (d) case 11.

In **Fig. 13**, the isosurfaces of each term with a constant value of $1e^6$ (colored by the viscosity magnitude) are plotted for a more detailed analysis. The first column corresponds to the case where the inlet pressure is reduced significantly; thus, the flow is more viscous dominant. In the other columns, the same parameter for cases with identical pressure conditions but variable inlet temperatures is plotted. As **Fig. 13** shows, all the terms show a contribution to the nonsymmetric patterns. For the case with a higher Kn number (case 8), these non-axisymmetric patterns fade away. For the case with a lower Kn number, these patterns tend to be more chaotic. Therefore, no patterns consistent with the scour patterns can be highlighted with this isosurface. However, the middle columns show a condition with similar patterns as was discussed in **Fig. 2**. Notably, the pressure on Mars is almost identical to that of the earth and very different from the almost vacuum condition of the Moon. Therefore, such patterns could be observed during the landing on Mars rather than on the Moon's surface.

The patterns of the viscous term are more consistent with the scour patterns in dusty cases. These two observations imply the stronger role of the viscous term in presence of such patterns. Variations of these patterns for the rest of the simulated time steps along with isometric views are provided in the Appendix. The time transient isosurfaces in the appendix state that the baroclinicity and stretching are more in effect in the initial evolution of flow while the viscous term is effective in almost the whole investigated time.

Fig. 14 shows the isosurface of baroclinicity, dilatation, and viscous terms with different magnitudes at different time steps. In the supplementary material, the isosurfaces with 3 different magnitudes and for all the time steps and all the terms are provided. The figures in the supplementary materials show that both dilatation and baroclinicity terms have a role in such pattern formation, although the contribution is small. The viscous term has a more

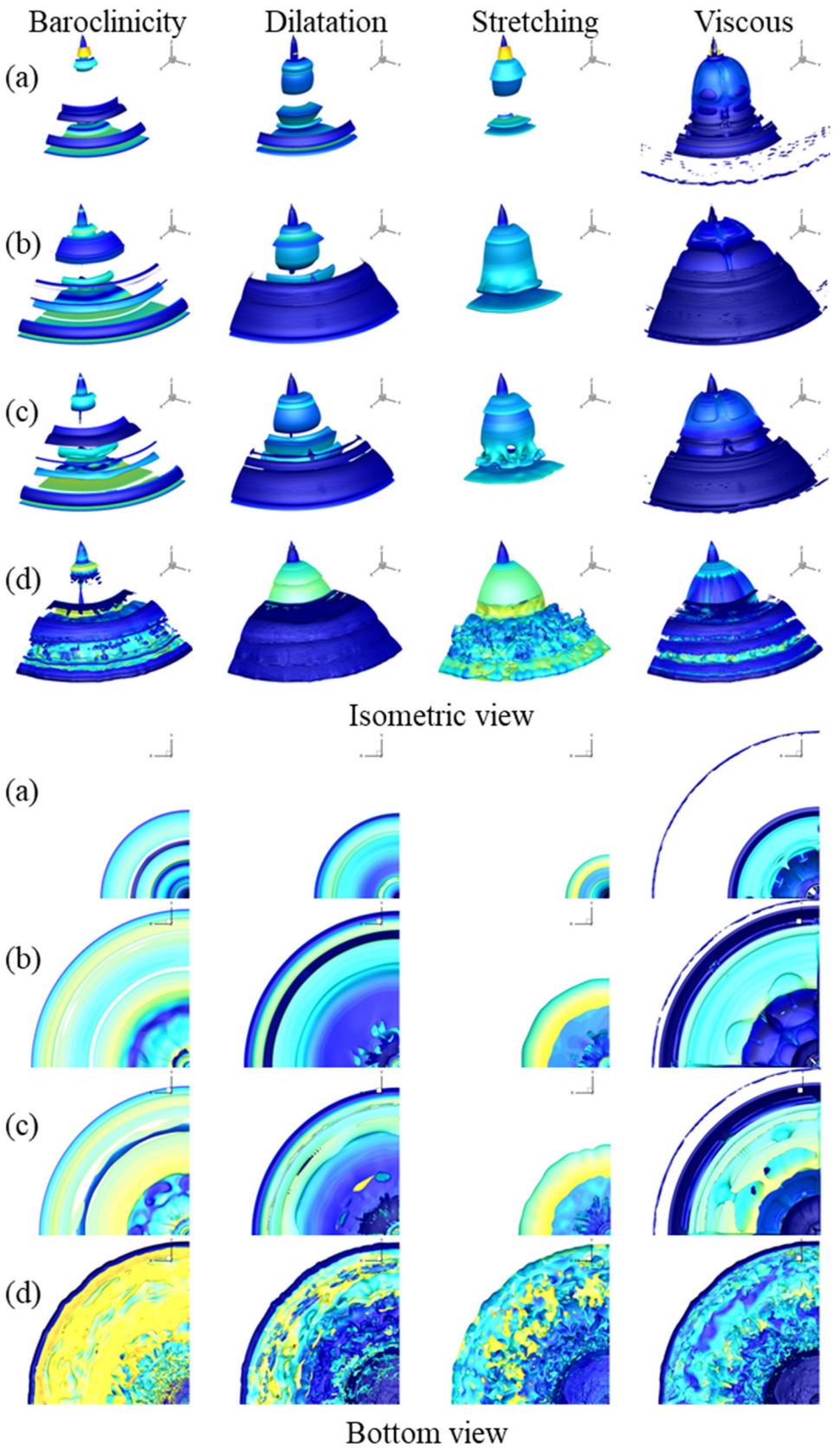

Fig. 13 Qualitative comparison of the topology of the isosurfaces of the different terms of VTE for t = 0.006 s: (a) baroclinicity; (b) dilatation; (c) stretching; (d) viscous.

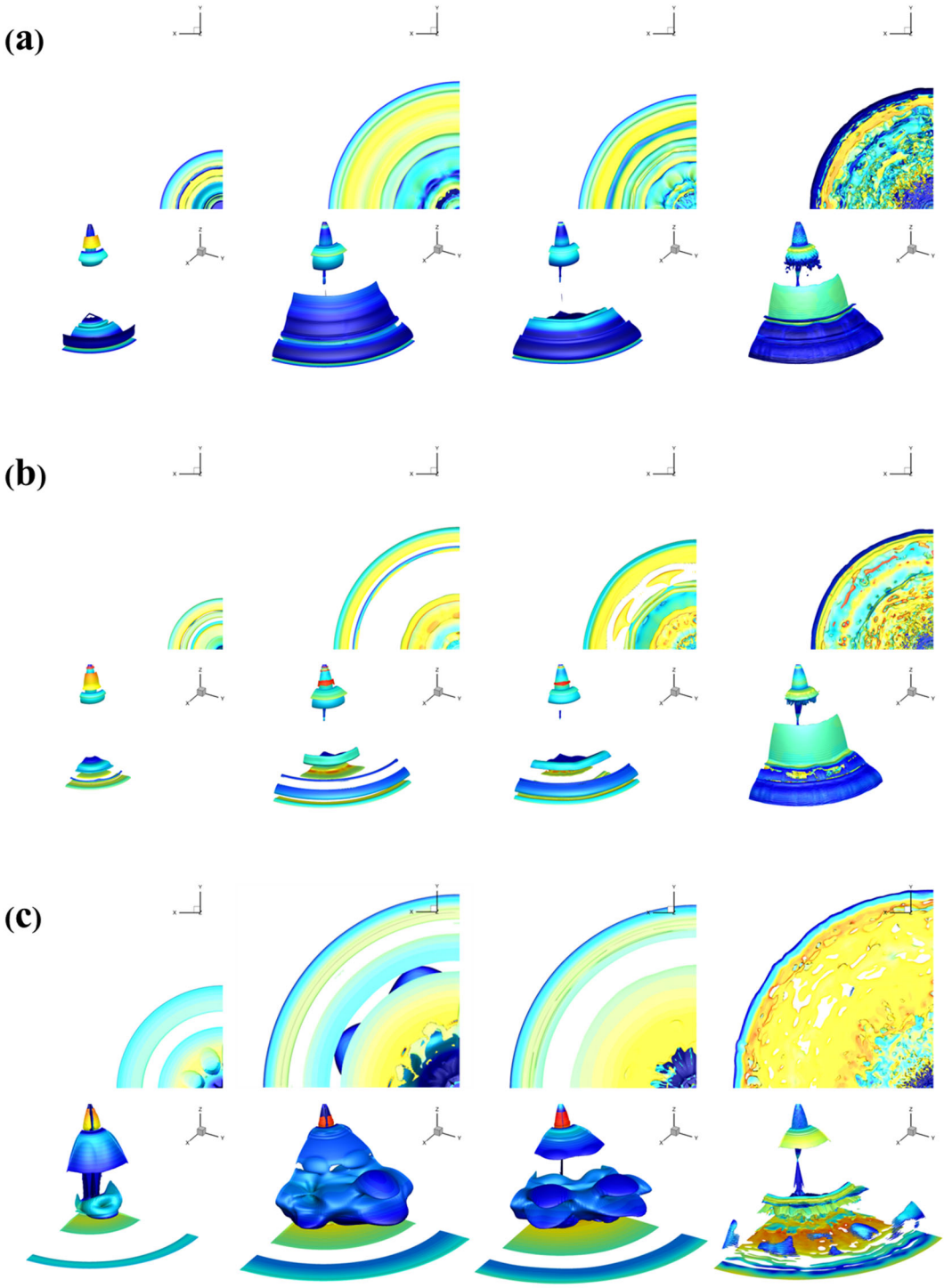

Fig. 14 Qualitative comparison of the topology of the different isosurfaces at different time steps: (a) 10^6 isosurface of baroclinicity term at $t = 0.004$ s, (b) 10^7 isosurface of dilatation term at $t = 0.004$ s, and (a) 10^7 isosurface of viscous term at $t = 0.008$ s.

dominant effect (highlighted in 10^7 isosurfaces) for cases 9 and 10. The isosurfaces and the time steps plotted in **Fig. 14** are those that can better represent the counterintuitive patterns and support for the aforementioned observation.

B. Dusty gas (two-phase) simulations

Here, we investigate some of the particulate phase parameters that can affect the scour patterns and the dispersion of the particles into the flowfield. In the Apollo mission videos, reduction of pilot visibility owing to the presence of dust has been documented. The contour plots in this section are presented in such a way that they reflect the inflight visibility restriction, also known as brownout. **Table 3** is a summary of the simulated cases in this section.

Table 3 Gas-solid multiphase simulations.

Test case	Particulate loading (β)	Particle diameter [μm]	Bed height [m]
1	1000	10	0.5
2	100	10	0.5
3	10	10	0.5
4	1	10	0.5
5	1000	1	0.5
6	1000	5	0.5
7	1000	10	0.5
8	1000	20	0.5
9	1000	50	0.5
10	1000	10	0.25
11	1000	10	1

1. Loading effects

Fig. 15 illustrates the effect of variation on the particulate loading of the bed. As can be observed with the decrease in the loading, the shape of the scour is affected significantly. The angle by which the ejecta is dispersed into the flowfield also depends on the loading, the higher the loading the lower the ejection angle. Additionally, it is observed that for lower particle loadings the bed is swept away faster.

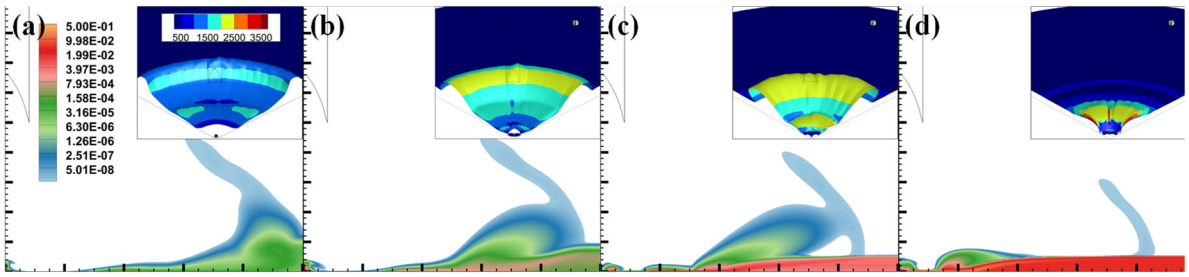

Fig. 15 Effect of variation of particulate loading (a) $\beta = 1000$, (b) $\beta = 100$, (c) $\beta = 10$, (d) $\beta = 1$, and $t = 0.01$ s.

2. Particle diameter effects

The effect of variation of particle diameters is also investigated. The diameter size of the particle is directly related to the Stokes number of the multiphase flow that characterizes the level of interaction of gas and particles, defined as the ratio of the relaxation time of the particles to the time scale of the fluid flow [51],

$$St = \frac{\tau_V}{t_{ref}}. \tag{24}$$

$$\tau_V = \frac{\rho_s d^2}{18\mu_g}, \tag{25}$$

where t_{ref} is the reference time, which can be defined as the characteristic length divided by the characteristic speed, and τ_V is the momentum response time of the particles. [51]

When small diameter particles are present, i.e. small Stokes number ($St \ll 1$), the particulate phase will be in dynamic equilibrium with the carrier phase. Conversely, larger particles, i.e., large Stokes number flow ($St \gg 1$), remain unaffected by the carrier phase, owing to their large inertia. **Fig. 16** shows how the variation can affect the topology of the particle dispersion in the flowfield (left column) and the scour pattern by the isosurfaces of the density (right column). Here, four particle diameter sizes (5 μm, 10 μm, 20 μm, and 50 μm) are simulated. As shown in the figure, particles smaller than 10 μm follow the gas streamlines (almost identical streamlines are observed for the 5 μm and 10 μm particles). A vortex is observed underneath the nozzle and some particles are trapped in this vortex; for the 50 μm particles, the interaction

of the particulate and gaseous phases leads to the disappearance of the vortex. This can explain the annulus shape of the crater observed in some of the simulations and experiments. The 20 μm case can be considered as an intermediate case where the vortex is not formed but a reverse flow towards the axis is still visible. In the investigated time, smaller particles are lifted up more than the larger particles. The density isosurface in the figure shows that the patterns on the bed with small particle sizes are identical (the shorter response time of the small particles allows them to follow the gas phase). The isosurface of the case of 20 μm is an intermediate case between particles following the gas phase and particles following a path close to its previous history. As can be observed, the presence of non-axisymmetric features in figure **Fig. 16 (d)** is less pronounced, which can support the observations in the previous section describing the nature of the counter-intuitive patterns to be originated from the gas phase.

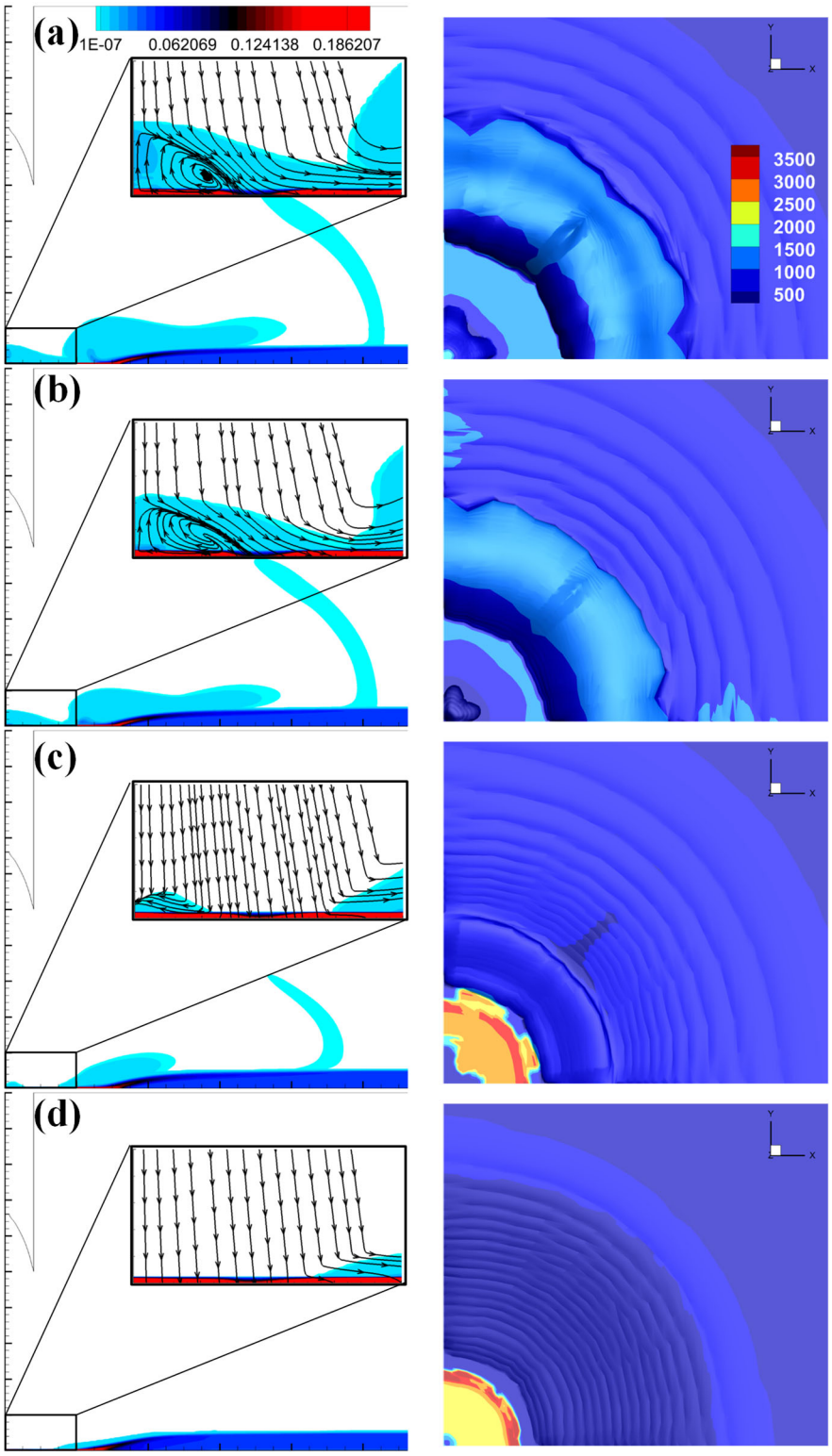

Fig. 16 Effect of variation of particle diameter for β = 1000: (a) d = 5 μm, (b) d = 10 μm, (c) d = 20 μm, (d) d = 50 μm, and t = 0.01 s. Left: solid density (kg/m^3) contour on symmetry plane, right: iso surface of solid density colored by the solid velocity (m/s) from top view.

3. Regolith bed height

Another parameter that can affect the scour pattern and the level of brownout is the dust bed height. Such effects are investigated in **Fig. 17** for two particle diameters (5 and 50 μm) and three heights (0.25, 0.5, and 1 m). An overall look at the density contours of the solid density on the symmetry plane (left column) reveals that small particles and beds with smaller heights are more susceptible to causing brownout owing to dust off.

Additionally, it can be observed that different scenarios lead to different gas velocity contours (middle column), meaning two-way coupling effects are strongly in effect, specifically for small diameter particles. When the bed height is 1 m, fewer particles are eroded and the maximum axial velocity is reduced; therefore, it takes longer for the jet to develop in the radial direction. The other feature that can be revealed is that the counter-intuitive scour patterns are more likely to appear for smaller particle sizes, which can follow the gas phase much easier owing to a shorter response time.

In beds with higher heights, the developing plume pushes the top layers of regolith toward the surface leading to an accumulation of solid particles in the axial direction before the flow develops in the radial direction. This is equivalent to the higher loading condition that was discussed in previous sections. As discussed in section IV.B.1, the higher the loading of the bed the slower the scouring of the bed. Therefore, less number of particles are dispersed into the flowfield before the plume develops in radian and upward (towards nozzle) directions which results in less brownout. The other factor that plays a role in here is the two-way coupling of the phases and how the solid phase affects the gaseous phases. Higher particulate loadings and larger particle diameters may distort the morphology of the plume and consequently, the core vortex that is generated beneath the nozzle, therefore, the erosion and dispersal of dust particles will be substantially different.

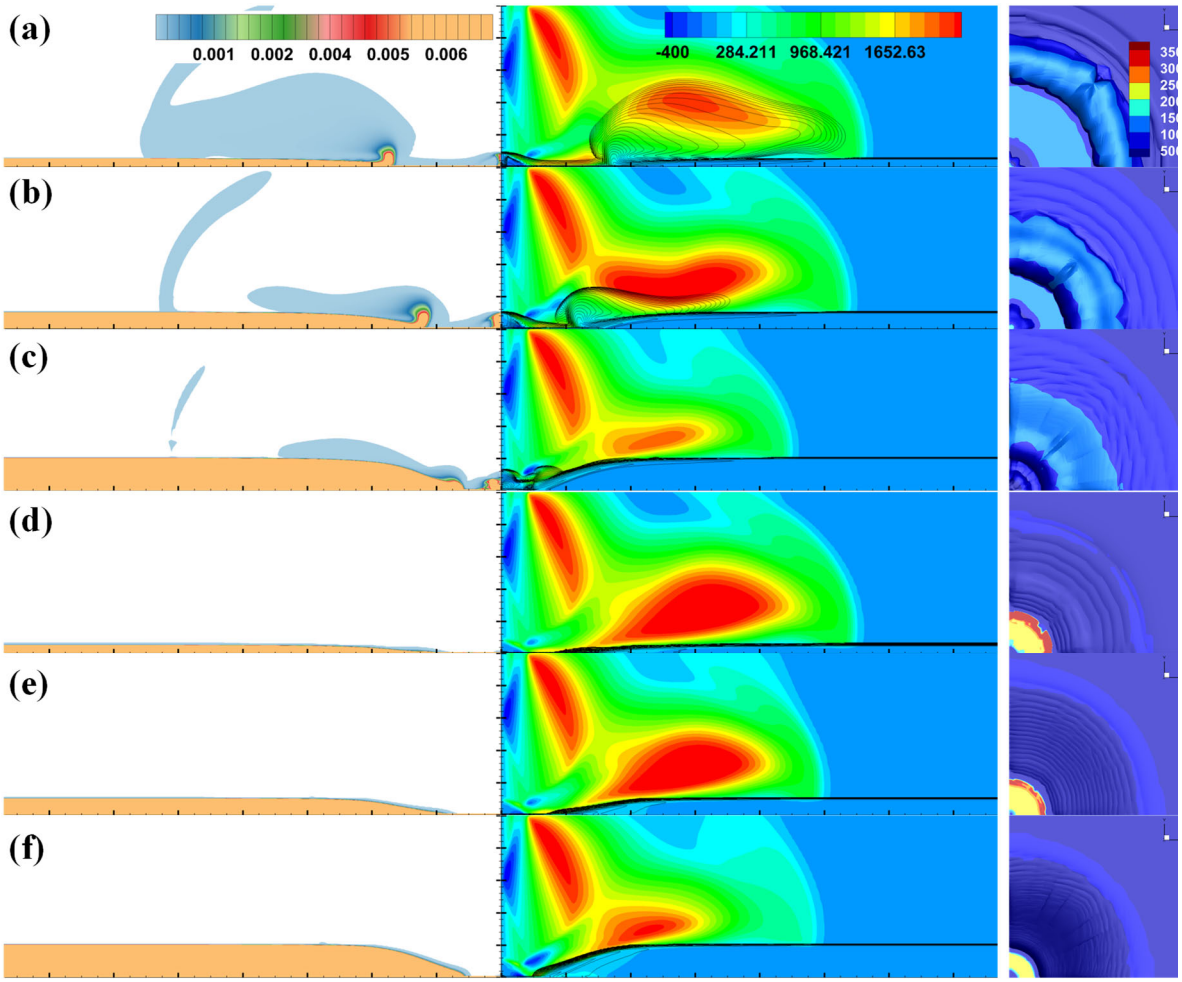

Fig. 17 Parametric study on the height of the dusty bed for two different particle diameters: 5 μm (a to c) and 50 μm (d to f). Left: solid density (kg/m^3) contours on symmetry plane, middle: radial velocity of gas contours overlaid on solid density lines on symmetry plane, right: top view of an isosurface of solid density colored by the velocity (m/s).

V. CONCLUSIONS

In this study, a full continuum framework for simulating a descent/ascend phase of planetary landing where the interaction of a plume with a bed of particles in an almost vacuum ambient condition was developed using a finite volume approach. The severe consequences of dust on the interstitial bodies are well established, and the difficulty of setting up experiments for simulating such scenarios highlights the importance of the developed tool. The methodology in the present study utilizes an Eulerian-Eulerian approach for modeling multiphase physics, which is computationally more efficient than the Lagrangian counterparts. Compared to the existing works in the literature, the developed framework benefits from a moment method

approach for simulating the rarefied flow. The tool can suit both the purpose of studying the PSI problem at the fundamental level (e.g., scour pattern formation, and development of erosion models) and more practical engineering applications (e.g., prediction of the particle trajectories to avoid damage to the lander and previously established sites and also planning the descend/ascend scenarios). Even though the DSMC method is a very ideal candidate for simulating this problem and in spite of the recent developments,[52, 53] the computational cost, makes the current framework a much more practical engineering tool.

The role of back pressure, dynamics, and bulk viscosities on the structure of the single-phase plume, i.e., features such as the reflection point, shock standoff distance, and curvature were analyzed. Among the three parameters investigated and with the ranges under investigation, it was observed that the nozzle-to-ambient pressure ratio has the largest effect on the shock standoff morphology and its distance from the surface and has almost a negligible effect on the reflection point. On the other hand, dynamics and bulk viscosity have an almost negligible effect on the shock standoff distance, however, the variation of these parameters tends to change the curvature of the standoff shock. These parameters are also shown to dislocate the reflection point as well.

Furthermore, the vorticity transport equation terms were analyzed in detail to highlight the role of vortical structures on the non-counterintuitive scour patterns. The role of the viscous term was elaborated, it was demonstrated that although in the first stages of the flow development baroclinity and stretching terms also contribute to the festooned patterns, the viscous term has a more dominant effect during the entire simulated period. The single-phase simulations indicate that these patterns are not merely a consequence of interaction with the regolith but an inherent feature of the gaseous PSI.

The solid phase parameters were also analyzed and the effect of each parameter on the brownout phenomena and the dynamics of particle ejecta were summarized. It was discussed that the origin of the formation of annulus craters is directly related to the vortex beneath the nozzle, and the vortex strongly depends on solid phase properties. Particles with smaller diameters and beds with shorter heights and lower particulate loadings lead to the dispersion of particles to higher altitudes, therefore causing severe brownout during the ascend/descend phases. The axial compaction of the beds as the plume initially impinges on the bed and before

jet development in radial and upward directions is the reason for the more favorable brownout state of beds with larger heights.

The simulation of the farfield region necessitates devising a multiscale approach to deal with the different time and length scales. Proper measures to consider such types of simulations as well as the inclusion of solid particle collisions in the modeling and simulating cases with larger solid volume fractions will be followed in our future research.

ACKNOWLEDGMENTS

This work was supported by the National Research Foundation of Korea grants funded by the Ministry of Science and ICT (NRF 2022R1I1A1A01065532 and NRF 2022R1A4A1030333), South Korea. R.S.M. acknowledges the support from the National Research Foundation of Korea funded by the Ministry of Science and ICT (2022M1A3C2074536 Future Space Education Center), South Korea.

REFERENCES

[1] K. H. Lee, "Lunar Orbiter Trade Study and Conceptual Design of Onboard Propulsion System," Journal of Spacecraft and Rockets **48**, 346 (2011).

[2] J. Burt, and I. Boyd, *Development of a two-way coupled model for two phase rarefied flows* (2004).

[3] S. Gimelshein, A. Alexeenko, D. Wadsworth, and N. Gimelshein, *The influence of particulates on thruster plume/shock layer interaction at high altitudes* (2004).

[4] J. E. Lane, P. T. Metzger, and C. D. Immer, *Lagrangian trajectory modeling of lunar dust particles* (2008).

[5] P. Liever, A. Tosh, R. Arslanbekov, and S. Habchi, *Modeling of Rocket Plume Impingement Flow and Debris Transport in Lunar Environment* (2012).

[6] X. He, B. He, and G. Cai, "Simulation of rocket plume and lunar dust using DSMC method," Acta Astronautica **70**, 100 (2012).

[7] A. B. Morris, "Simulation of Rocket Plume Impingement and Dust Dispersal on the Lunar Surface," Doctoral dissertation The University of Texas at Austin, 2012.

[8] A. B. Morris, D. B. Goldstein, P. L. Varghese, and L. M. Trafton, "Approach for modeling rocket plume impingement and dust dispersal on the moon," Journal of Spacecraft and Rockets **52**, 362 (2015).

[9] Y. Li, D. Ren, Z. Bo, W. Huang, Q. Ye, and Y. Cui, "Gas-particle two-way coupled method for simulating the interaction between a rocket plume and lunar dust," Acta Astronautica **157**, 123 (2019).

[10] A. Rahimi, O. Ejtehadi, K. H. Lee, and R. S. Myong, "Near-field plume-surface interaction and regolith erosion and dispersal during the lunar landing," Acta Astronautica **175**, 308 (2020).

[11] A. K. Chinnappan, R. Kumar, and V. K. Arghode, "Modeling of dusty gas flows due to plume impingement on a lunar surface," Physics of Fluids **33**, 053307 (2021).

[12] D. Fontes, J. G. Mantovani, and P. Metzger, "Numerical estimations of lunar regolith trajectories and damage potential due to rocket plumes," Acta Astronautica **195**, 169 (2022).

[13] J. E. Vesper, T. J. M. Broeders, J. Batenburg, D. E. A. v. Odyck, and C. R. Kleijn, "The interaction of parallel and inclined planar rarefied sonic plumes—From free molecular to continuum regime," Physics of Fluids **33**, 086103 (2021).

[14] A. Capone, G. Moscato, and G. Romano, "Role of density ratio on particle dispersion in a turbulent jet," Physics of Fluids **35**, 013332 (2023).

[15] M. Fathi, S. Hickel, and D. Roekaerts, "Large eddy simulations of reacting and non-reacting transcritical fuel sprays using multiphase thermodynamics," Physics of Fluids **34**, 085131 (2022).

[16] O. Ejtehadi, and R. S. Myong, "A modal discontinuous Galerkin method for simulating dusty and granular gas flows in thermal non-equilibrium in the Eulerian framework," Journal of Computational Physics **411**, 109410 (2020).

[17] K. Balakrishnan, and J. Bellan, "High-fidelity modeling and numerical simulation of cratering induced by the interaction of a supersonic jet with a granular bed of solid particles," International Journal of Multiphase Flow **99**, 1 (2018).

[18] MSL, *https://mars.nasa.gov/msl-raw-images/msss/00000/mrdi/0000MD9999000526E1_DXXX.jpg* (2012).

[19] R. Scott, and H. Y. Ko, "Transient rocket-engine gas flow in soil," AIAA Journal **6**, 258 (1968).

[20] O. Ejtehadi, T. Mankodi, I. Sohn, R. S. Myong, and B. J. Kim, "Investigation of the non-equilibrium two-phase flow of gas and particles in a microscale shock tube and jet impingement on a permeable surface," Under review.

[21] O. Ejtehadi, A. Rahimi, A. Karchani, and R. Myong, "Complex wave patterns in dilute gas–particle flows based on a novel discontinuous Galerkin scheme," International Journal of Multiphase Flow **104**, 125 (2018).

[22] O. Ejtehadi, A. Rahimi, and R. S. Myong, "Numerical investigation of the counter-intuitive behavior of Mach disk movement in underexpanded gas-particle jets," Journal of Computational Fluid Engineering **24**, 19 (2019).

[23] O. Ejtehadi, and R. S. Myong, "Eulerian-Eulerian simulation of dusty gas flows past a prism from subsonic to supersonic regimes using a modal discontinuous Galerkin method," Computers & Fluids **218**, 104841 (2021).

[24] O. Ejtehadi, A. Rahimi, and R. S. Myong, "Investigation of a trifold interaction mechanism of shock, vortex, and dust using a DG method in a two-fluid model framework," Powder Technology **374**, 121 (2020).

[25] O. Ejtehadi, E. Mahravan, and I. Sohn, "Investigation of shock and a dust cloud interaction in Eulerian framework using a newly developed OpenFOAM solver," International Journal of Multiphase Flow **145**, 103812 (2021).

[26] C. Lun, S. B. Savage, D. Jeffrey, and N. Chepurniy, “Kinetic theories for granular flow: inelastic particles in Couette flow and slightly inelastic particles in a general flowfield,” Journal of fluid mechanics **140**, 223 (1984).

[27] M. Reeks, “On the constitutive relations for dispersed particles in nonuniform flows. I: Dispersion in a simple shear flow,” Physics of Fluids A: Fluid Dynamics **5**, 750 (1993).

[28] D. Gidaspow, *Multiphase Flow and Fluidization: Continuum and Kinetic Theory Descriptions* (Academic press, 1994).

[29] A. Busch, and S. T. Johansen, “On the validity of the two-fluid-KTGF approach for dense gravity-driven granular flows,” Powder Technology (2020).

[30] C. Curtiss, “The classical Boltzmann equation of a gas of diatomic molecules,” The Journal of Chemical Physics **75**, 376 (1981).

[31] R. S. Myong, “A computational method for Eu's generalized hydrodynamic equations of rarefied and microscale gasdynamics,” Journal of Computational Physics **168**, 47 (2001).

[32] R. S. Myong, “Coupled nonlinear constitutive models for rarefied and microscale gas flows: subtle interplay of kinematics and dissipation effects,” Continuum Mechanics and Thermodynamics **21**, 389 (2009).

[33] R. S. Myong, “On the high Mach number shock structure singularity caused by overreach of Maxwellian molecules,” Physics of Fluids **26**, 056102 (2014).

[34] B. C. Eu, *Kinetic Theory and Irreversible Thermodynamics* (John Wiley and Sons, Inc., 1992).

[35] B. C. Eu, and Y. G. Ohr, “Generalized hydrodynamics, bulk viscosity, and sound wave absorption and dispersion in dilute rigid molecular gases,” Physics of Fluids **13**, 744 (2001).

[36] L. Onsager, “Reciprocal relations in irreversible processes. I,” Physical review **37**, 405 (1931).

[37] H. Xiao, R. S. Myong, and S. Singh, “A new near-equilibrium breakdown parameter based on the Rayleigh-Onsager dissipation function,” AIP Conference Proceedings **1628**, 527 (2014).

[38] R. S. Myong, “A generalized hydrodynamic computational model for rarefied and microscale diatomic gas flows,” Journal of Computational Physics **195**, 655 (2004).

[39] R. S. Myong, *Numerical Simulation of Hypersonic Rarefied Flows Using the Second-Order Constitutive Model of the Boltzmann Equation* (InTech, 2018).

[40] S. Singh, M. Battiato, and R. S. Myong, “Impact of bulk viscosity on flow morphology of shock-accelerated cylindrical light bubble in diatomic and polyatomic gases,” Physics of Fluids **33**, 066103 (2021).

[41] A. Koop, "Numerical Simulation of Unsteady Three-dimensional Sheet Cavitation (University of Twente) Ph. D," thesis, 2008.

[42] T. J. Barth, and D. C. Jespersen, *The design and application of upwind schemes on unstructured meshes* (American Institute of Aeronautics and Astronautics, 1989).

[43] K. G. Powell, P. L. Roe, R. S. Myong, and T. Gombosi, *An upwind scheme for magnetohydrodynamics* (1995).

[44] K. G. Powell, P. L. Roe, T. J. Linde, T. I. Gombosi, and D. L. De Zeeuw, "A solution-adaptive upwind scheme for ideal magnetohydrodynamics," Journal of Computational Physics **154**, 284 (1999).

[45] P. Janhunen, "A positive conservative method for magnetohydrodynamics based on HLL and Roe methods," Journal of Computational Physics **160**, 649 (2000).

[46] S. Jung, and R. Myong, "A second-order positivity-preserving finite volume upwind scheme for air-mixed droplet flow in atmospheric icing," Computers & Fluids **86**, 459 (2013).

[47] T. Chourushi, A. Rahimi, S. Singh, O. Ejtehadi, T. K. Mankodi, and R. S. Myong, "Thermal and flow characteristics of nonequilibrium monatomic, diatomic, and polyatomic gases in cylindrical Couette flow based on second-order non-Navier–Fourier constitutive model," International Journal of Heat and Mass Transfer **187**, 122580 (2022).

[48] S. Singh, A. Karchani, T. Chourushi, and R. S. Myong, "A three-dimensional modal discontinuous Galerkin method for the second-order Boltzmann-Curtiss-based constitutive model of rarefied and microscale gas flows," Journal of Computational Physics **457**, 111052 (2022).

[49] O. Ejtehadi, Tapan K. Mankodi, I. Sohn, and R. S. Myong, "Flow and thermal characteristics of two-phase flow of diatomic gas and solid particles in microscale shock tube," Physics of Fluids (Under Prepration).

[50] T. K. Mankodi, O. Ejtehadi, T. Chourushi, A. Rahimi, and R. S. Myong, "nccrFOAM suite: Nonlinear coupled constitutive relation solver in OpenFOAM framework for rarefied and microscale gas flows with vibrational non-equilibrium," Under review (Under review).

[51] C. T. Crowe, *Multiphase Flow Handbook* (CRC press, 2005).

[52] S. Stefanov, E. Roohi, and A. Shoja-Sani, "A novel transient-adaptive subcell algorithm with a hybrid application of different collision techniques in direct simulation Monte Carlo (DSMC)," Physics of Fluids **34**, 092003 (2022).

[53] R. S. Myong, A. Karchani, and O. Ejtehadi, "A review and perspective on a convergence analysis of the direct simulation Monte Carlo and solution verification," Physics of Fluids **31**, 066101 (2019).

SUPPLEMENTARY MATERIAL

A. Isosurfaces of VTE terms

In this supplementary document, the isosurfaces of the four main vorticity mechanisms in the vorticity transport equation at different time steps and for three different cases are plotted. The columns from right to left correspond to cases 8 to 11 of **Table 2**. Each row represents a time step and isosurfaces are provided by a 0.002 s gap.

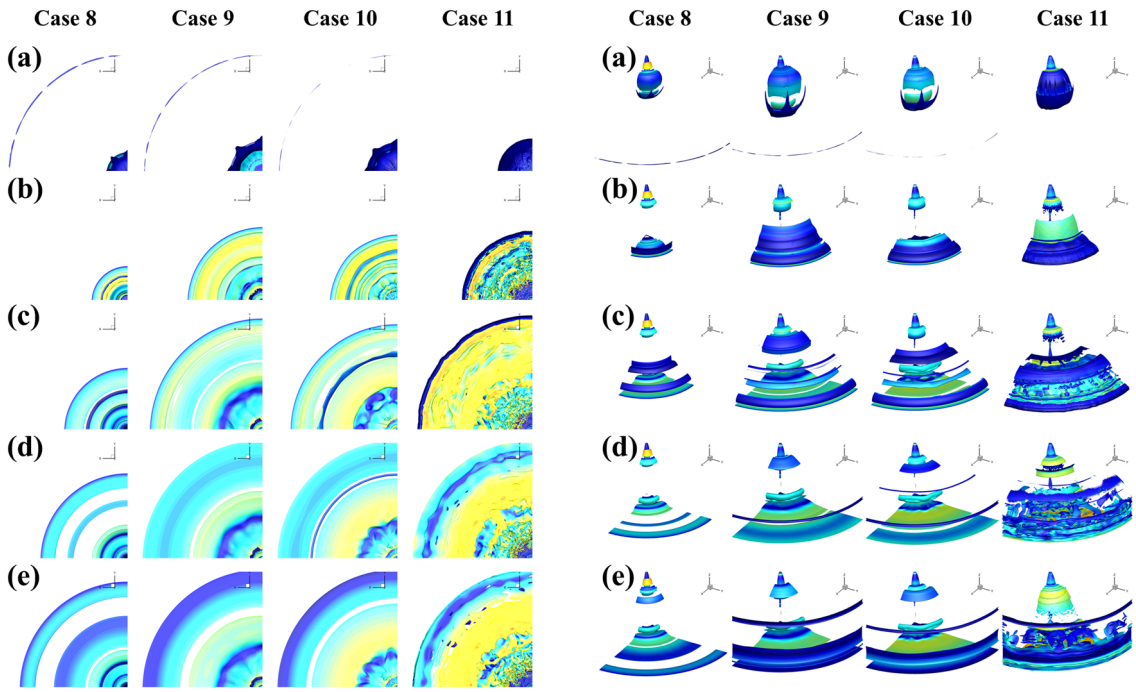

Fig. S. 1 Isosurfaces of the baroclinicity term (10^6) at different time steps for four cases: (a) t = 2 ms; (b) t = 4 ms; (c) t = 6 ms; (d) t = 8 ms; (e) t = 10 ms.

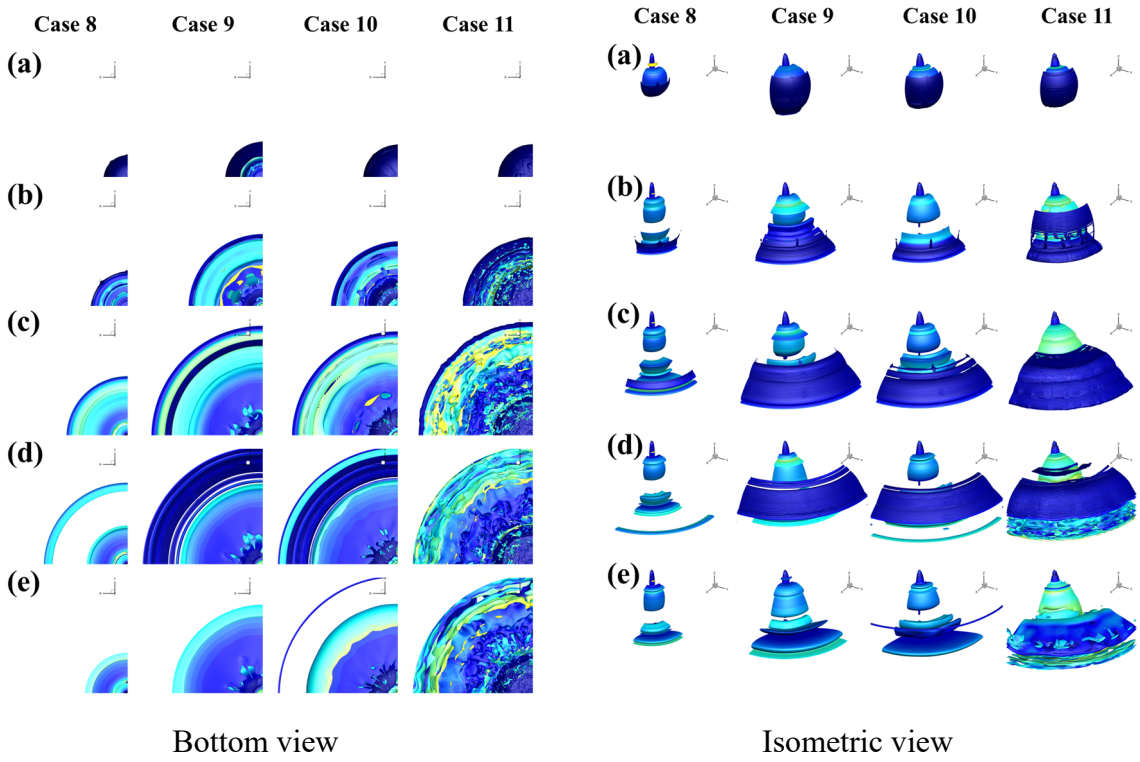

Fig. S. 2 Isosurfaces of the dilatation term (10^6) at different time steps for four cases: (a) t = 2 ms; (b) t = 4 ms; (c) t = 6 ms; (d) t = 8 ms; (e) t = 10 ms.

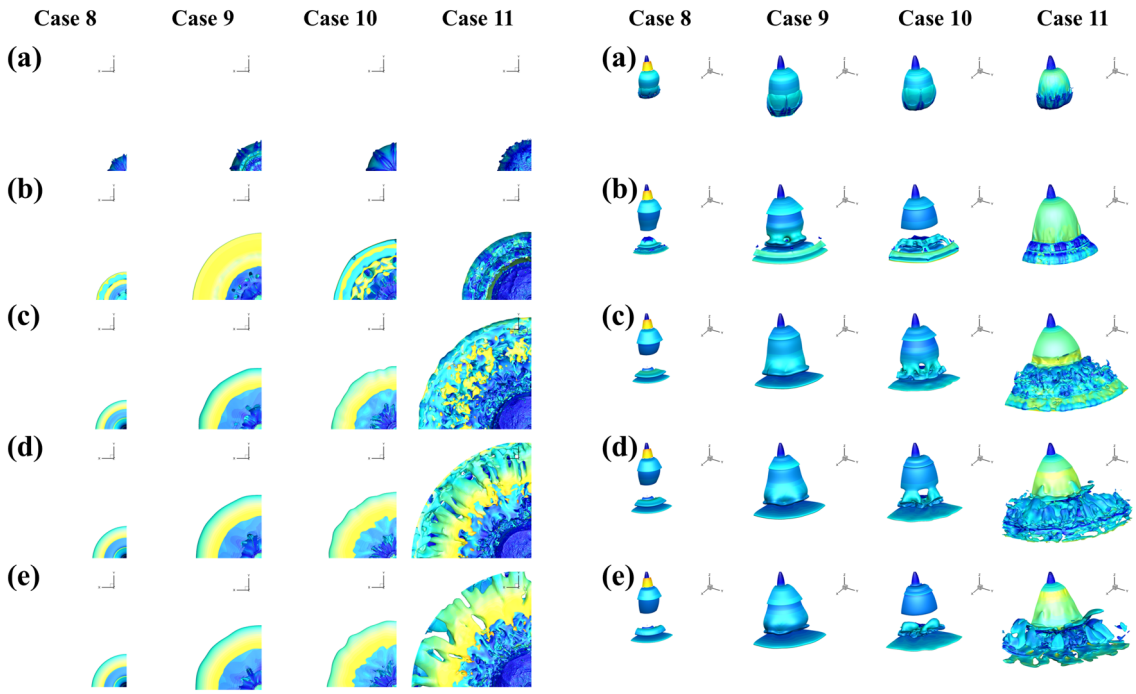

Fig. S. 3 Isosurfaces of the stretching term (10^6) at different time steps for four cases: (a) t = 2 ms; (b) t = 4 ms; (c) t = 6 ms; (d) t = 8 ms; (e) t = 10 ms.

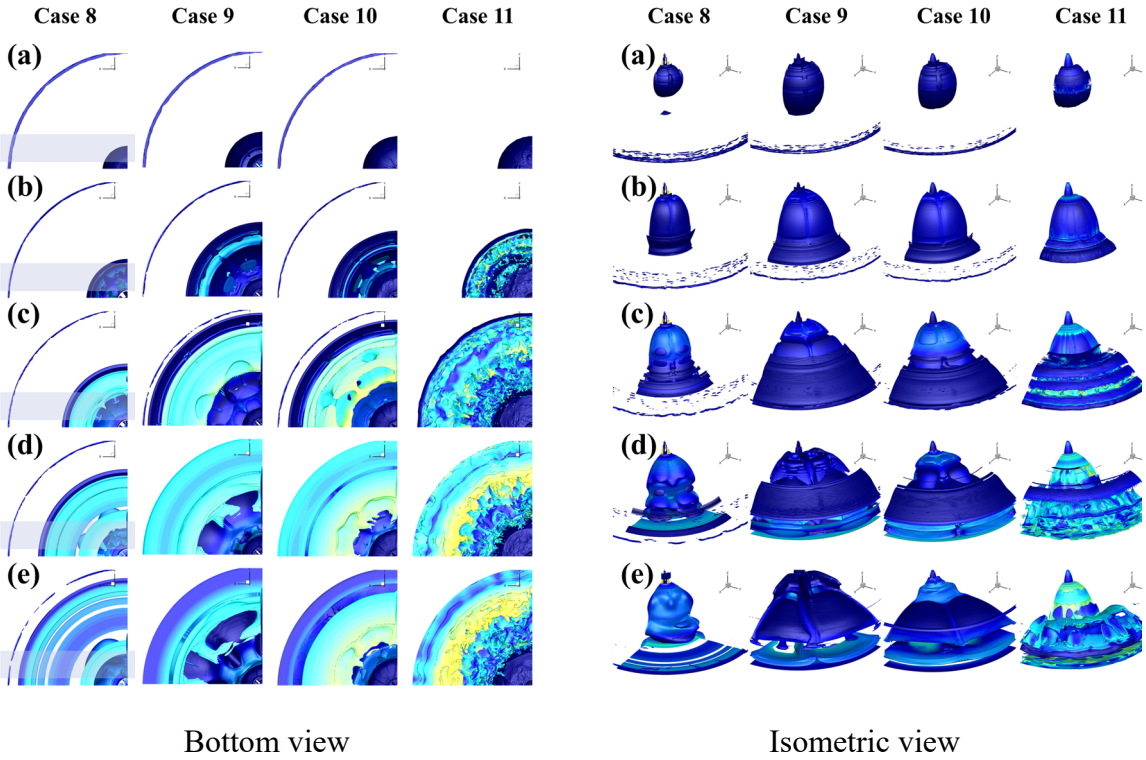

Fig. S. 4 Isosurfaces of the viscous term (10^6) at different time steps for four cases: (a) t = 2 ms; (b) t = 4 ms; (c) t = 6 ms; (d) t = 8 ms; (e) t = 10 ms.

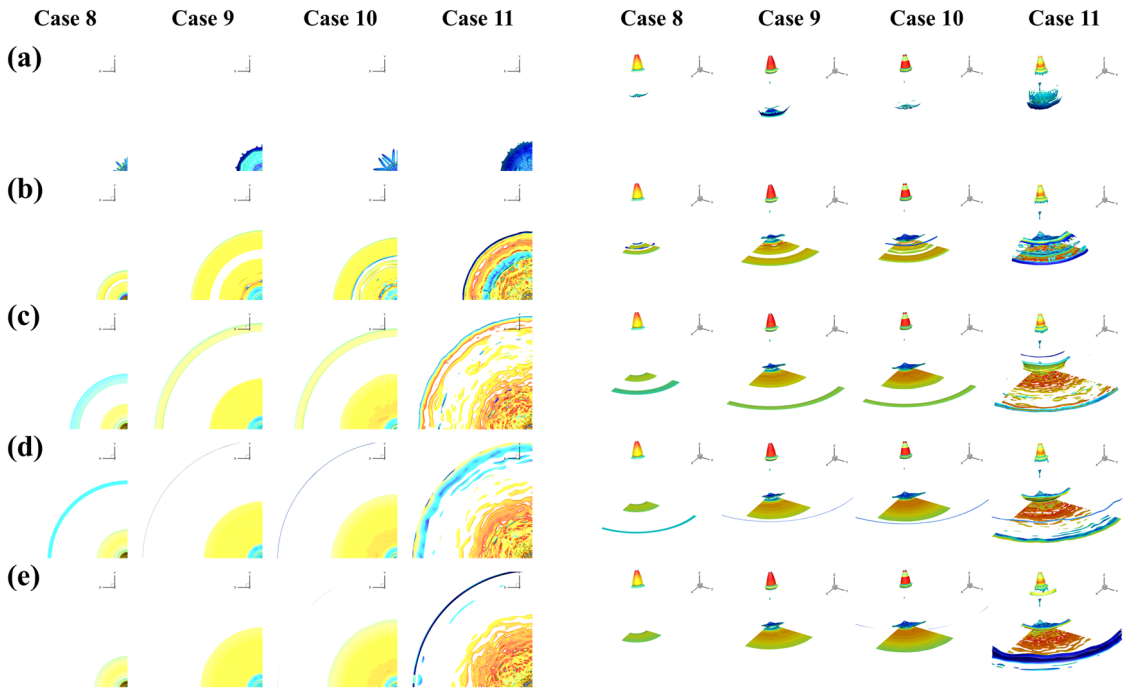

Bottom view Isometric view

Fig. S. 5 Isosurfaces of the baroclinicity term (10^7) at different time steps for four cases: (a) t = 2 ms; (b) t = 4 ms; (c) t = 6 ms; (d) t = 8 ms; (e) t = 10 ms.

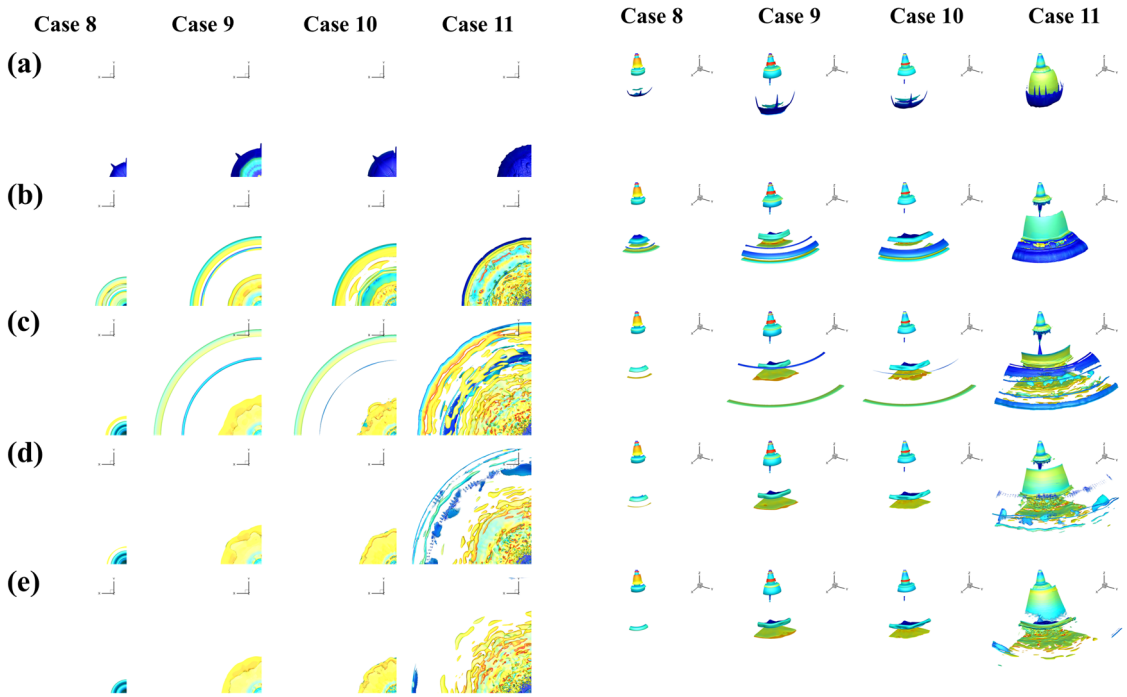

Bottom view Isometric view

Fig. S. 6 Isosurfaces of the dilatation term (10^7) at different time steps for four cases: (a) t = 2 ms; (b) t = 4 ms; (c) t = 6 ms; (d) t = 8 ms; (e) t = 10 ms.

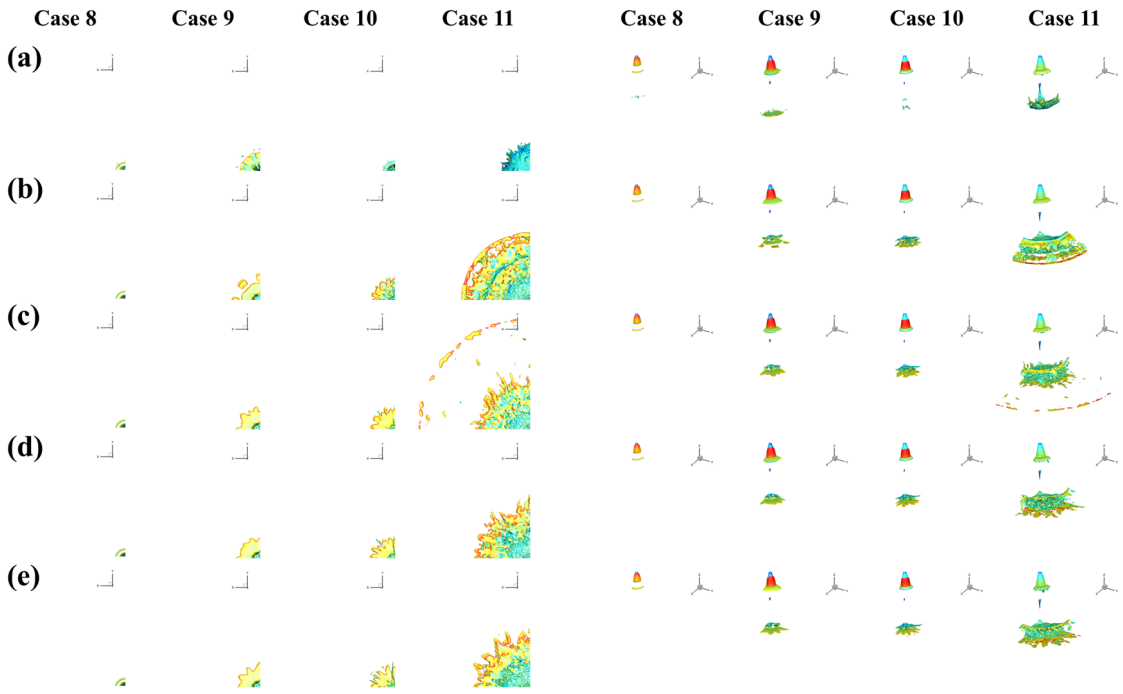

Fig. S. 7 Isosurfaces of the stretching term (10^7) at different time steps for four cases: (a) t = 2 ms; (b) t = 4 ms; (c) t = 6 ms; (d) t = 8 ms; (e) t = 10 ms.

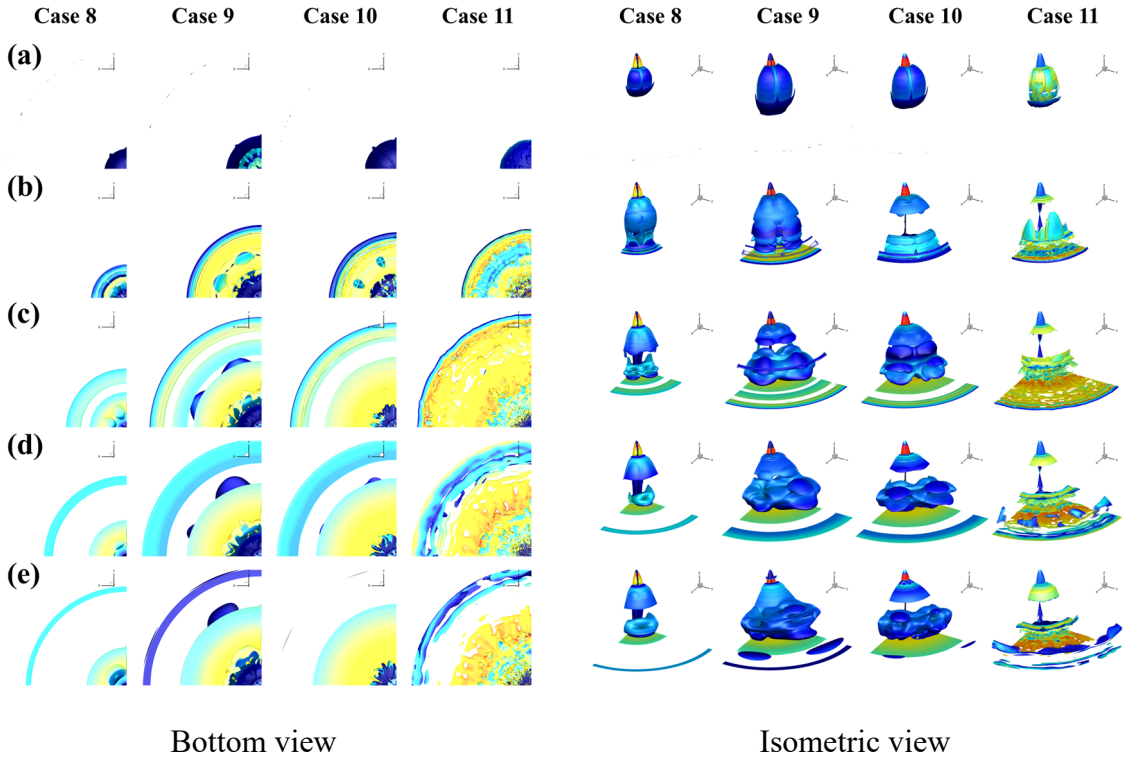

Fig. S. 8 Isosurfaces of the viscous term (10^7) at different time steps for four cases: (a) t = 2 ms; (b) t = 4 ms; (c) t = 6 ms; (d) t = 8 ms; (e) t = 10 ms.

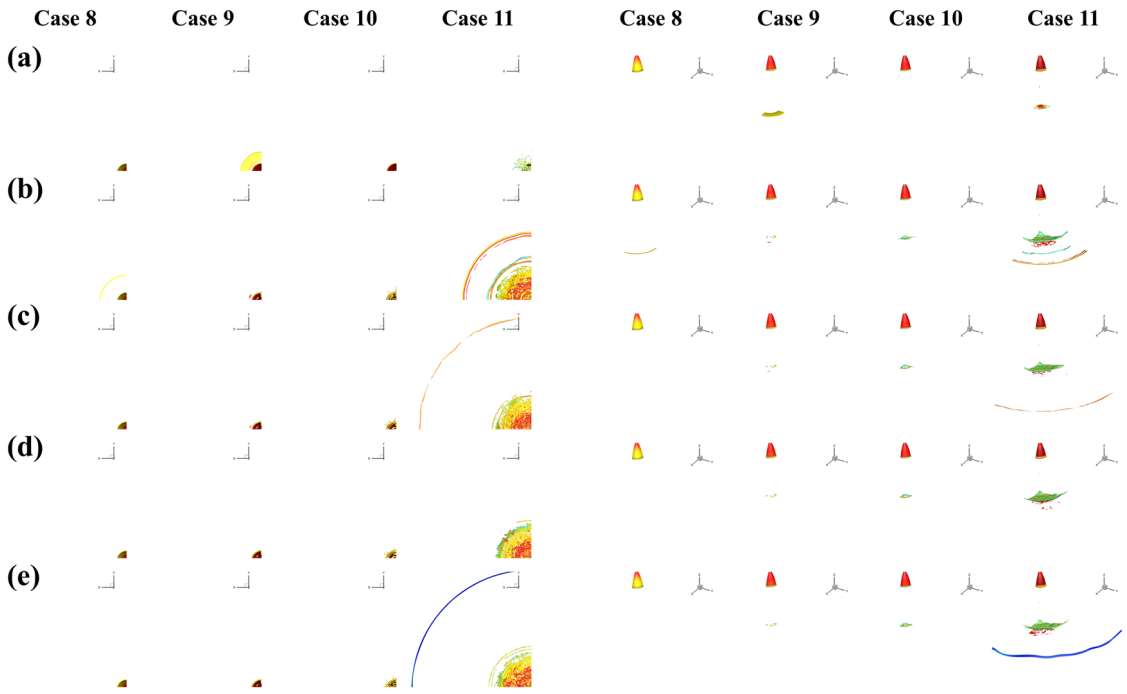

Fig. S. 9 Isosurfaces of the baroclinicity term (10^8) at different time steps for four cases: (a) t = 2 ms; (b) t = 4 ms; (c) t = 6 ms; (d) t = 8 ms; (e) t = 10 ms.

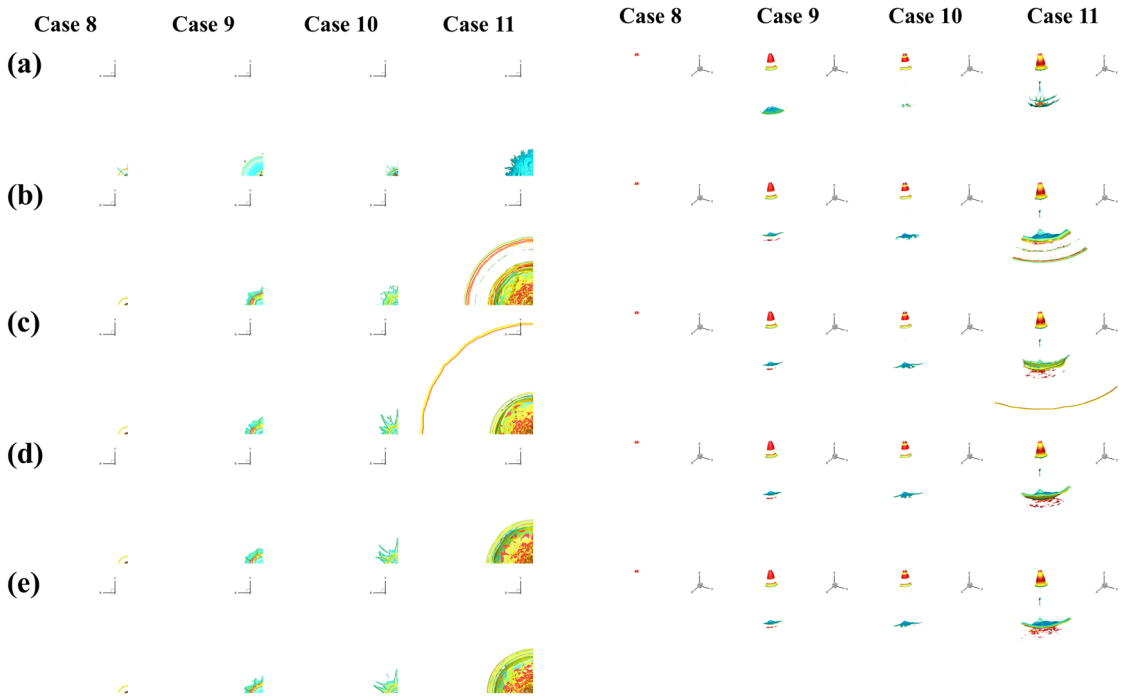

Fig. S. 10 Isosurfaces of the dilatation term (10^8) at different time steps for four cases: (a) t = 2 ms; (b) t = 4 ms; (c) t = 6 ms; (d) t = 8 ms; (e) t = 10 ms.

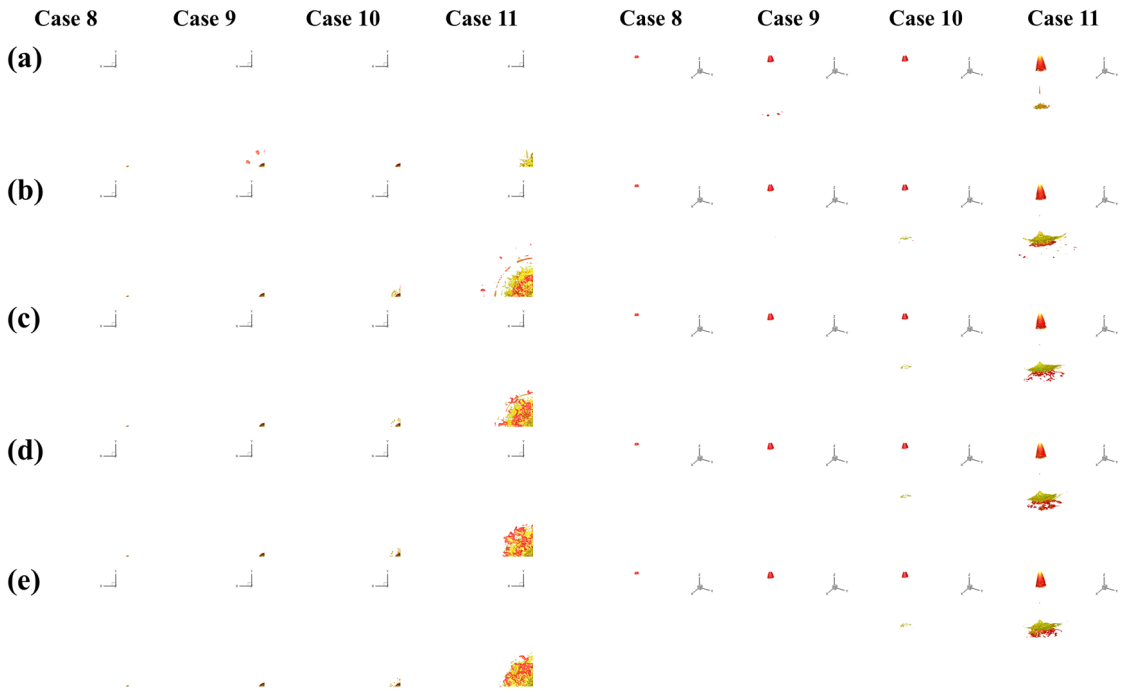

Fig. S. 11 Isosurfaces of the stretching term (10^8) at different time steps for four cases: (a) t = 2 ms; (b) t = 4 ms; (c) t = 6 ms; (d) t = 8 ms; (e) t = 10 ms.

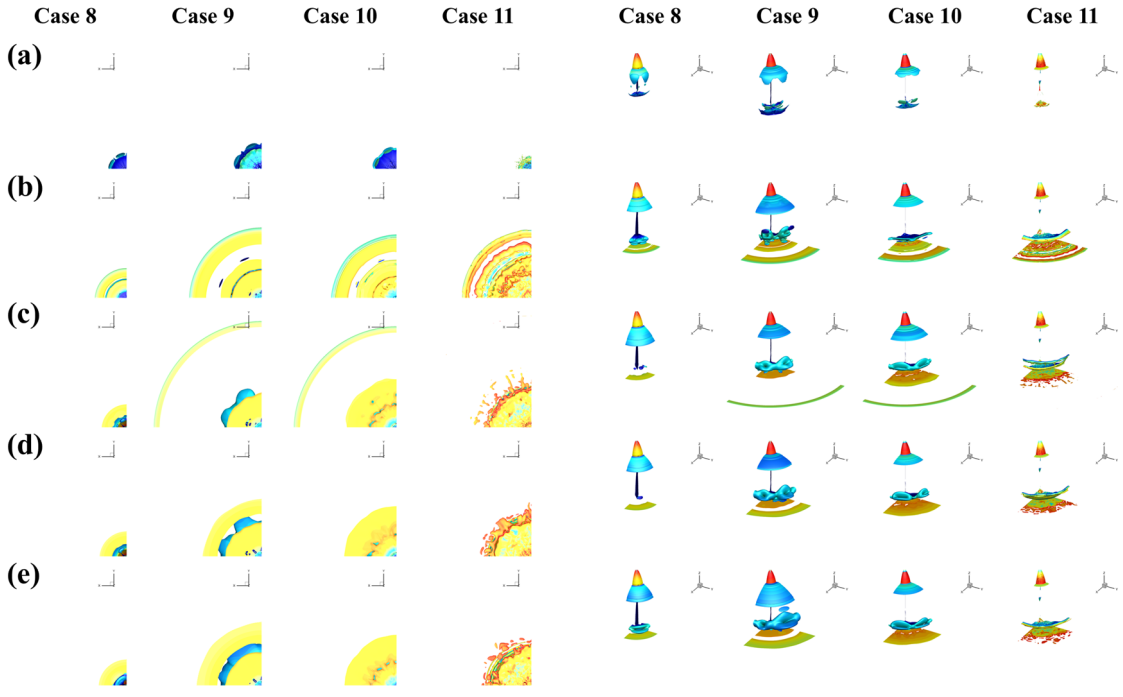

Fig. S. 12 Isosurfaces of the viscous term (10^8) at different time steps for four cases: (a) (a) t = 2 ms; (b) t = 4 ms; (c) t = 6 ms; (d) t = 8 ms; (e) t = 10 ms.

B. Cross-sections of vorticity magnitude

The figure below shows the vorticity snapshots of the cases 8 to 11 of **Table 2** at various heights and times steps.

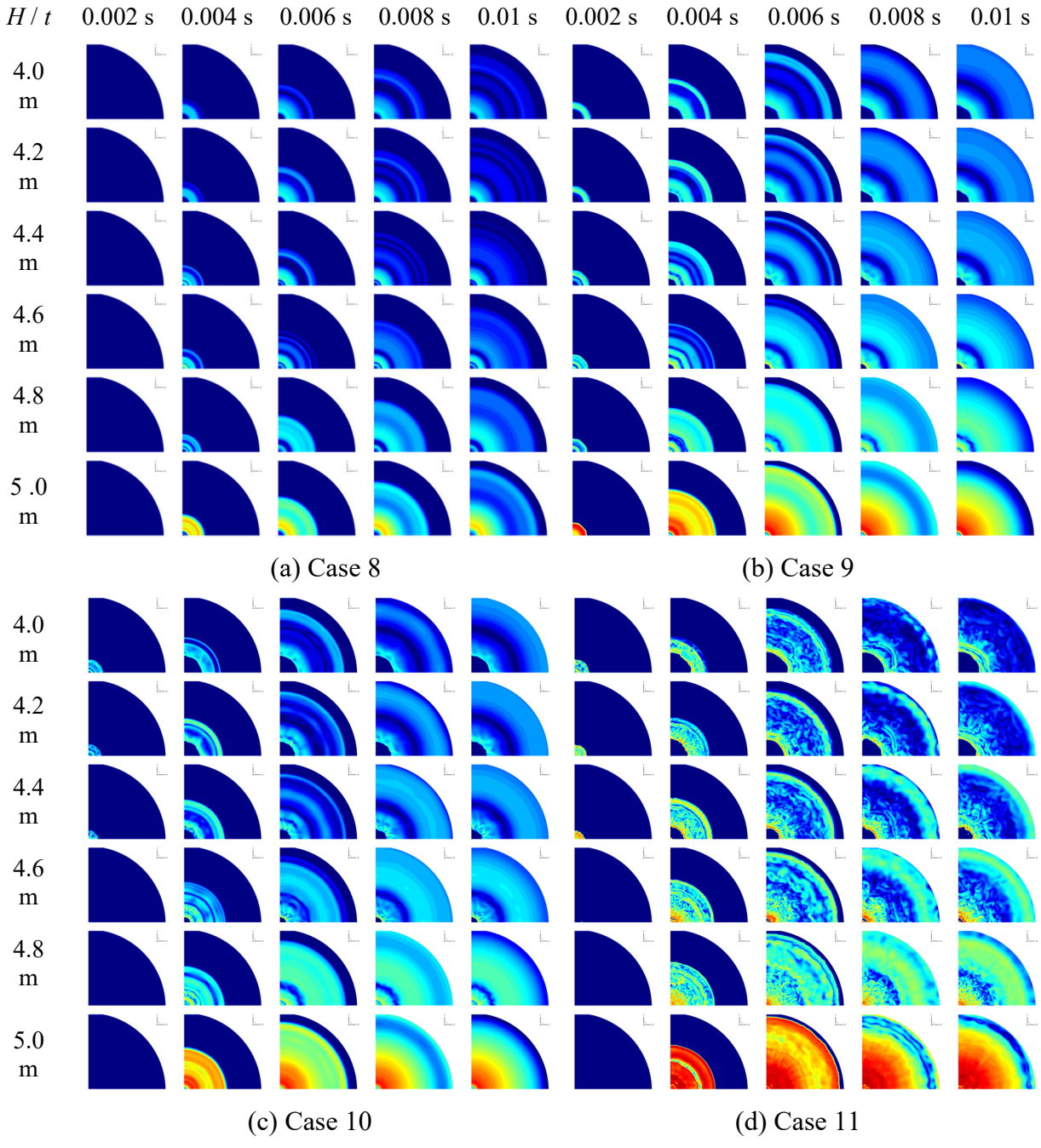

Fig. S. 13 Vorticity snapshots at different heights and time steps.